

Equation of State Dependence of Gravitational Waves in Core-Collapse Supernovae

OLIVER EGGENBERGER ANDERSEN ¹, SHUAI ZHA ¹, ANDRÉ DA SILVA SCHNEIDER ¹, AURORE BETRANHANDY ¹,
SEAN M. COUCH ^{2,3,4} AND EVAN P. O'CONNOR ¹

¹*The Oskar Klein Centre, Department of Astronomy,
Stockholm University, AlbaNova, SE-106 91 Stockholm, Sweden*

²*Department of Physics and Astronomy, Michigan State University, East Lansing, MI 48824, USA;*

³*Department of Computational Mathematics, Science, and Engineering, Michigan State University, East Lansing, MI 48824, USA*

⁴*Facility for Rare Isotope Beams, Michigan State University, East Lansing, MI 48824, USA*

ABSTRACT

Gravitational waves (GWs) provide unobscured insight into the birthplace of neutron stars (NSs) and black holes in core-collapse supernovae (CCSNe). The nuclear equation of state (EOS) describing these dense environments is yet uncertain, and variations in its prescription affect the proto-neutron star (PNS) and the post-bounce dynamics in CCSNe simulations, subsequently impacting the GW emission. We perform axisymmetric simulations of CCSNe with Skyrme-type EOSs to study how the GW signal and PNS convection zone are impacted by two experimentally accessible EOS parameters, (1) the effective mass of nucleons, m^* , which is crucial in setting the thermal dependence of the EOS, and (2) the isoscalar incompressibility modulus, K_{sat} . While K_{sat} shows little impact, the peak frequency of the GWs has a strong effective mass dependence due to faster contraction of the PNS for higher values of m^* owing to a decreased thermal pressure. These more compact PNSs also exhibit more neutrino heating which drives earlier explosions and correlates with the GW amplitude via accretion plumes striking the PNS, exciting the oscillations. We investigate the spatial origin of the GWs and show the agreement between a frequency-radial distribution of the GW emission and a perturbation analysis. We do not rule out overshoot from below via PNS convection as another moderately strong excitation mechanism in our simulations. We also study the combined effect of effective mass and rotation. In all our simulations we find evidence for a power gap near ~ 1250 Hz, we investigate its origin and report its EOS dependence.

1. INTRODUCTION

Core-collapse supernovae (CCSNe) are the extraordinary birth sites of neutron stars (NSs) and stellar-mass black holes (BHs) and are triggered from the gravitational collapse of a massive star. During a CCSN, a proto-neutron star (PNS) forms where the iron core of the massive star once was. In a PNS, which subsequently evolves into a NS or a BH, matter exists in a wide range of temperatures, $0 \lesssim T \lesssim \mathcal{O}(100 \text{ MeV})$, can be compressed to densities up to and beyond $\rho \simeq 10^{15} \text{ g cm}^{-3}$, and may be proton rich, $y \simeq 0.6$, or very neutron rich, $y \simeq 0$, where y is the ratio of protons to baryons. As some of these conditions are rarely found elsewhere in the Universe, PNSs are unique probes of matter in its most extreme states. However, PNSs are hidden from our direct sight by the outer layers of the massive star. Thus, only neutrinos and gravitational waves (GWs) produced in the aftermath of the core collapse of a massive star can provide unobscured insight into these extreme environments.

As the recent detection of gravitational waves from merging binary systems of BHs (e.g. Abbott et al. 2016) and NSs (Abbott et al. 2017) marks the onset of GW interferometer astronomy, hope arises that the next major breakthrough comes from a multimessenger event of a nearby CCSN (Szczepanczyk et al. 2021). Since the estimated Galactic CCSN rate is $3_{-2.6}^{+7.3}$ per century (Li et al. 2011; Adams et al. 2013), such hope is scientifically justified. The yield of knowledge from such an event is bounded by our understanding of CCSNe and the description of dense nuclear matter. The nuclear equation of state (EOS) is one of the fundamental ingredients for predicting the dynamics of CCSNe. The spectra of neutrinos, the PNS mass, its radius, cooling rate, and the GW signal are all dependent on the EOS. As details and parameters in the EOS of dense nuclear matter are yet poorly constrained (Oertel et al. 2017), a wide range of EOSs are typically used in CCSNe simulations (Hempel et al. 2017). As a result, there are several studies exploring the dependence of the GW emission on

the nuclear EOS (Kuroda et al. 2017; Pan et al. 2018; Morozova et al. 2018), however, due to the large nuclear EOS model space available and the diversity of available EOSs in this model space, disentangling the impact of individual EOS parameters on the CCSN dynamics must be done carefully.

Despite differences in microphysics and model construction, some of these EOSs can be characterized in terms of semi-analytic, semi-experimental empirical parameters defined via a Taylor expansion about saturation density (Oertel et al. 2017; Margueron et al. 2018). This approach, referred to as meta-modeling, was used by Schneider et al. (2019) to construct a set of finite-temperature EOSs based on the framework developed by Lattimer et al. (1985); Lattimer & Swesty (1991); Schneider et al. (2017). These EOSs describe nucleon interactions via a Skyrme force and the thermal contributions in the homogeneous phases, regions of parameter space where heavy nuclei do not appear, are fully determined by the effective mass of nucleons.

In a comprehensive set of spherically-symmetric CC-SNe simulations (and also limited 3D simulations) of the $20-M_{\odot}$ progenitor star of Woosley & Heger (2007), Schneider et al. (2019) report an effective mass dependence of the post-bounce dynamics. As the effective mass serves as a proxy for the EOS temperature dependence, changing its value affects the thermal pressure throughout the PNS. In fact, increasing the value of the effective mass parameter leads to a decrease in thermal pressure in the core of the PNS. Less thermal support from the core renders the PNS more compact and its outer regions, where the neutrinosphere is located, hotter. A hotter and more compact neutrinosphere emits higher energy neutrinos with an increased luminosity and neutrino heating which drives stronger convection and turbulence in the gain region and facilitates successful SN explosions (Schneider et al. 2019; Yasin et al. 2020). Higher turbulence and convection in the gain region has been suggested to impact PNS oscillations, and therefore potentially influence the amplitude of the GWs (Murphy et al. 2009; O’Connor & Couch 2018a). Explosion dynamics aside, the compactness of the PNS is one of the main factors that determines the frequency of the GWs (Müller et al. 2013; Pan et al. 2018; Morozova et al. 2018). Thus, a study of the thermal effects on the gravitational wave signal from the core-collapse of massive stars is opportune and is carried out here. We find a substantial impact of the effective mass on the peak GW frequency and its evolution through these aforementioned thermal effects.

Recent efforts in understanding the nature of gravitational wave emission from CCSNe has also revealed, in

some simulations, the presence of a “power gap” in the frequency spectrum of the emitted gravitational wave signal. As first noted by Morozova et al. (2018), the power gap is a narrow ($\Delta f \sim 50$ Hz), high frequency (~ 1200 Hz) persistent (100s of ms in duration) lack of GW power that is present from the onset of GW emission. Morozova et al. (2018) suggest this gap has its origins in an interaction between trapped modes in the PNS core and higher frequency p-modes present in the outer parts of the PNS. As such, it is likely linked to the eventual transition of the dominant GW emission from that of a core g-mode to a higher-frequency mode, either the f-mode (Sotani & Takiwaki 2020; Morozova et al. 2018) or another g-mode Torres-Forné et al. (2019a). It remains to be seen whether this GW spectral feature is physical in nature, and what, if any, is its EOS dependence. We note, from the public availability of GW signals from CCSNe (with sufficient data to capture signals at ~ 1300 Hz), that the presence of this power gap is also seen in the 3D simulations of O’Connor & Couch (2018a) and Radice et al. (2019), but not in the 3D simulation of Mezzacappa et al. (2020). We report on the presence of the power gap in our simulations presented here and explore its nature.

Related to the question of the presence and origin of the GW spectrum power gap is the origin of the GWs themselves. There is tension in the literature regarding the location in PNS where the GWs are emitted. By decomposing the gravitational wave signal into its radial dependence, Mezzacappa et al. (2020) suggests the bulk of the emission in their 3D simulation arises from inside the PNS convection zone. This is supported to some extent by the work of Andresen et al. (2017), who decompose the signal into the contribution from the PNS convection zone (and its overshoot layer), the convectively-stable PNS surface zone, and the gain region. Andresen et al. (2017) find in their 3D models that the emission was predominantly coming from the PNS convection and overshoot layer and little emission was coming from the stable PNS layer itself. However, they note that the majority of the emission comes from the small overshoot region directly at the base of this layer and at the top of PNS convection layer. Similar analysis in Andresen et al. (2017) of axisymmetric (2D) models, shows the potential for (perhaps unphysically) large GW emission in the convectively-stable PNS layer, however, this is not always present in the 2D simulations they study and may be associated with the presence of a strong standing accretion shock instability (SASI). In this article, we perform an in-depth analysis of the spatial origin of the GW emission. We find evidence for the peak GW emission occurring in the convective overshoot

layer at the top of the PNS convection zone, supporting the findings of [Andresen et al. \(2017\)](#). However, we note that the global nature of the GW emission, whose radial profile agrees with the results of a perturbation analysis, suggests that a precise determination of the PNS excitation mechanism via the spatial location of the GW emission alone may not be possible.

In this paper, we perform 2D axisymmetric simulations of CCSNe to investigate the impact of the effective mass and the incompressibility modulus of the EOS on the post-bounce GW signal. We also study the combined effect of rotation and effective mass. With this suite of simulations we also investigate the origin of the power gap and the spatial origin of the GW emission. The paper is organized in the following way. In § 2 we outline the numerical setup, equation of states used, and how we extract the GW signal from our numerical simulations. In § 3 we present our results on the dependence of the GW emission on the effective mass (§3.1), rotation (§3.2), incompressibility (§3.3), spatial origin (§3.4), and present our investigation of the power gap (§3.5). We summarize and conclude in §4.

2. METHODS

2.1. Numerical Setup

Each stellar core collapse simulation we perform uses a progenitor with zero-age main sequence mass of $20 M_{\odot}$ from [Woosley & Heger \(2007\)](#) and is started at the onset of collapse in our 2D domain. We utilize the FLASH (v.4) multiscale, multiphysics adaptive mesh refinement framework ([Fryxell et al. 2000](#)) modified for core-collapse in [Couch \(2013\)](#); [Couch & O’Connor \(2014\)](#); [O’Connor & Couch \(2018b\)](#). The grid setup is a 2D cylindrical geometry that spans 1×10^9 cm in the radial direction and $\pm 1 \times 10^9$ cm along the cylindrical axis. Our maximum block size is 2×10^8 cm and we allow a total of 10 levels of mesh refinement, giving a minimum block size of ~ 3.9 km and minimum grid zone spacing of ~ 326 m. Beyond 80 km, the highest level of refinement is limited so as to only maintain an angular resolution of $0^{\circ}.82$. We use standard Newtonian hydrodynamics and solve gravity by employing a modified general relativistic effective potential (case A) for the monopole contribution ([Marek et al. 2006](#)), retaining spherical harmonic orders up to 16. We note that the use of an effective potential leads to, in general, a quantitative over-prediction of the GW frequency due to the inconsistency of the underlying Newtonian hydrodynamics ([Müller et al. 2013](#); [Zha et al. 2020](#)).

We incorporate a multidimensional, multispecies and energy dependent neutrino transport following an M1 scheme outlined in [O’Connor & Couch \(2018b\)](#). As

such, we distinguish three species of neutrino i.e., electron neutrinos, ν_e , electron anti-neutrinos $\bar{\nu}_e$, and the composite group of heavy lepton neutrinos/anti-neutrinos ν_x . For each EOS employed, a set of neutrino opacities is generated using the neutrino transport library NuLib ([O’Connor 2015](#)). Neutrino opacities are computed for 12 logarithmically-spaced energy groups, the first group centered on 1 MeV and the last one centered on ~ 315 MeV. For the emission of electron type neutrinos and anti-neutrinos, we include electron and positron capture interactions on protons and neutrons, respectively, as well as electron capture on heavy nuclei following [Bruenn \(1985\)](#). For the emission of heavy lepton neutrino pairs we include emission from electron-positron annihilation to $\nu\bar{\nu}$ pairs following [Bruenn \(1985\)](#) and nucleon-nucleon bremsstrahlung following [Burrows et al. \(2006\)](#); [Hannestad & Raffelt \(1998\)](#). We include these pair emissions in a parameterized way ([Betranhandy & O’Connor 2020](#)). We include isoenergetic scattering of neutrinos of all types on nucleons, nuclei, and alpha particles following [Bruenn \(1985\)](#). For the charged-current interactions on nucleons as well as the neutral-current scattering interactions we include corrections for weak-magnetism following [Horowitz \(2002\)](#). We also include inelastic scattering of neutrinos on electrons following [Bruenn \(1985\)](#).

For the simulations that include rotation, we map the progenitor model onto the cylindrical grid via an artificial rotation profile,

$$\Omega(r) = \Omega_0 \left[1 + \left(\frac{r}{A} \right)^2 \right]^{-1}, \quad (1)$$

where $r = \sqrt{z^2 + R^2}$ is the spherical radius for a given cylindrical radius R and symmetry axis coordinate z , Ω_0 is the central angular speed of the star, and A the differential rotation parameter. Using this same scheme, [Pajkos et al. \(2019\)](#) find that the parameter A strongly correlates with the stellar core compactness ([O’Connor & Ott 2011](#)), and calculate an optimal value of $A = 1021$ km for the compactness $\xi_{2.5} = 0.2785$ of the $20 M_{\odot}$ progenitor used here.

2.2. Equation of State

We use five EOSs from [Schneider et al. \(2019\)](#) who constructed 97 Skyrme-type EOSs using the open-source code SROEOS ([Schneider et al. 2017](#)). [Schneider et al. \(2019\)](#) take pair-wise combinations of 8 empirically accessible parameters and allow them to vary within their estimated uncertainties based on current nuclear physics constraints ([Danielewicz et al. 2002](#); [Margueron et al. 2018](#)). The EOSs are based on the commonly used “liquid-drop model” framework of [Lattimer et al. \(1985\)](#);

Lattimer & Swesty (1991) where nucleon interactions are computed via a Skyrme force. SROEOS has some improvements with respect to the model of Lattimer & Swesty (1991); the most relevant to this paper being that SROEOS (1) allows simple variations of the effective mass of nucleons instead of fixing them at their vacuum values and (2) the ability to compute EOSs for any desired value of the isoscalar incompressibility modulus K_{sat} rather than limiting them to 180, 220, and 375 MeV baryon $^{-1}$.

In this paper, we focus on variations in two empirical parameters to determine their effect on GW signatures. First, we focus on the effective mass of symmetric nuclear matter at saturation density, $m^* = m_n^*(n = n_{\text{sat}}, y = 1/2) \simeq m_p^*(n_{\text{sat}}, 1/2)$ ¹, where n is the baryon number density, $n_{\text{sat}} = 0.155 \text{ fm}^{-3}$, y the proton fraction, and the subscripts n and p denote neutrons and protons, respectively. Second, we adjust the isoscalar incompressibility modulus K_{sat} . We motivate this choice of parameters by their seemingly largest effect on the PNS radius in Schneider et al. (2019), followed by the isovector incompressibility modulus K_{sym} . We note that the effect on PNS structure of m^* is much more significant than that of K_{sat} and, thus, we expect a similar correlation in our results.

In Skyrme-type models, the inverse of the nucleon effective masses have a simple linear relation with nucleon densities. They are computed from

$$\frac{\hbar^2}{2m_t^*} = \frac{\hbar^2}{2m_t} + \alpha_1 n_t + \alpha_2 n_{-t}, \quad (2)$$

where α_i are Skyrme parameters, m_t is the vacuum mass, and n_t are number densities of nucleon of type t . For n_t , if $t = n$ then $-t = p$ and vice versa. The parameters α_i are set to reproduce the desired effective mass behavior. We refer to Schneider et al. (2019) for further details. Note however that the finite-temperature component of the EOS is sensitive to the effective masses of nucleons (Prakash et al. 1997; Constantinou et al. 2014), while the incompressibility modulus enters as a parameter in the Taylor expansion around saturation density which describes the zero-temperature component (Margueron et al. 2018; Schneider et al. 2019). Thus, while K_{sat} (m_t^*) has a strong (weak) effect on the *cold* NS structure it has a weak (strong) effect on the structure of a hot PNS.

As in Schneider et al. (2019, 2020), we begin with a simulation where the EOS parameters assume a set of baseline values (see Table 1), in particular with $m^* =$

Quantity	Baseline	Variation 2σ	Unit
m^*	0.75	0.20	m_n
K_{sat}	230	30	MeV baryon $^{-1}$
n_{sat}	0.155		fm^{-3}
ϵ_{sat}	-15.8		MeV baryon $^{-1}$
ϵ_{sym}	32		MeV baryon $^{-1}$
L_{sym}	45		MeV baryon $^{-1}$
K_{sym}	-100		MeV baryon $^{-1}$
Δm^*	0.10		m_n
$P_{\text{SNM}}^{(4)}$	125		MeV fm^{-3}
$P_{\text{PNM}}^{(4)}$	200		MeV fm^{-3}

Table 1. Nuclear matter properties of the baseline EOS, following Schneider et al. (2020). See Schneider et al. (2019) for further details. 2σ variations are shown for the two parameters we investigate in this work.

0.75 (specified as a fraction of the neutron mass vacuum value) and $K_{\text{sat}} = 230 \text{ MeV baryon}^{-1}$. Next, we keep all but one parameter at baseline, varying it with 2σ above and below baseline. The 2σ values for m^* (K_{sat}) below baseline is 0.55 (200 MeV baryon $^{-1}$) and above baseline is 0.95 (260 MeV baryon $^{-1}$). For both $m^* = 0.55$ and $m^* = 0.95$, two additional simulations are performed including rotation with $\Omega_0 = 1 \text{ rad s}^{-1}$ and $\Omega_0 = 2 \text{ rad s}^{-1}$. See Table 2 for an overview of the nine simulations performed in this paper.

m^* [m_n]	K_{sat} [MeV baryon $^{-1}$]	Ω_0 [rad s $^{-1}$]	Label
0.75*	230*	0	m0.75/k230
0.55	230*	0	m0.55
0.95	230*	0	m0.95
0.55	230*	1	m0.55r1
0.95	230*	1	m0.95r1
0.55	230*	2	m0.55r2
0.95	230*	2	m0.95r2
0.75*	200	0	k200
0.75*	260	0	k260

Table 2. Overview of the simulations performed that vary in the effective mass parameter, rotation rate, and the isoscalar incompressibility modulus parameter. * values are the baseline from Table 1.

2.3. Gravitational Wave Extraction

To extract the GW signal measured by a distant observer, we adopt the standard formula utilizing the second time derivative of the trace-free quadrupole moment. This quadrupole moment in the slow motion,

¹ The small difference between $m_n^*(n_{\text{sat}}, 1/2)$ and $m_p^*(n_{\text{sat}}, 1/2)$ is due to the small neutron proton mass difference.

weak-field formalism is given by (Blanchet et al. 1990; Finn & Evans 1990),

$$I_{ij} = \int d^3x (x_i x_j - \frac{1}{3} x^2 \delta_{ij}) \rho(t, \vec{x}), \quad (3)$$

where the indices range over (x, y, z) , δ_{ij} is the Kronecker delta and ρ the source energy density. For axisymmetric sources, the only independent component of the quadrupole moment is I_{zz} . Unless otherwise stated (for example, in § 3.4), we compute the first derivative in terms of the fluid velocity, v_i , via the analytic expression (Reisswig et al. 2011),

$$\frac{dI_{ij}}{dt} = \int d^3x (x_i v_j + v_i x_j - 2/3 \delta_{ij} x_k v_k) \rho(t, \vec{x}), \quad (4)$$

and the second time derivative is computed numerically. The axisymmetric GW strain for an observer located at the equator a distance D away from the source is then given as (Blanchet et al. 1990; Finn & Evans 1990),

$$h_+(t, \vec{x}) = \frac{2}{D} \frac{G}{c^4} \frac{d^2}{dt^2} I_{zz}, \quad (5)$$

where G is the gravitational constant, c the speed of light.

The GW spectrograms are extracted by short-time Fourier transforming (STFT) the GW signal,

$$\tilde{S}(f, \tau) = \int_{-\infty}^{\infty} s(t) H(t - \tau) e^{-2\pi i f t} dt, \quad (6)$$

into its frequency domain f . τ is the time offset of the Hann window function $H(t - \tau)$ (see e.g. Murphy et al. 2009). The sampling frequency of our simulation output is $\sim 2 \times 10^6$ Hz, which is reduced in the post-processing to $\sim 20,000$ Hz. Unless otherwise stated, we use a Hann window width of 40 ms and compute STFTs with a $\Delta\tau$ of 3.6 ms.

To investigate the hypothetical detectability of our simulations, we calculate the dimensionless characteristic strain (Murphy et al. 2009),

$$h_{\text{char}} = \sqrt{\frac{2}{\pi^2} \frac{G}{c^3} \frac{1}{D^2} \frac{dE_{\text{GW}}}{df}}, \quad (7)$$

with the spectral energy density,

$$\frac{dE_{\text{GW}}}{df} = \frac{3}{5} \frac{G}{c^5} (2\pi f)^2 |\tilde{A}|^2, \quad (8)$$

where \tilde{A} denotes the Fourier transform of $d^2 I_{zz}/dt^2$.

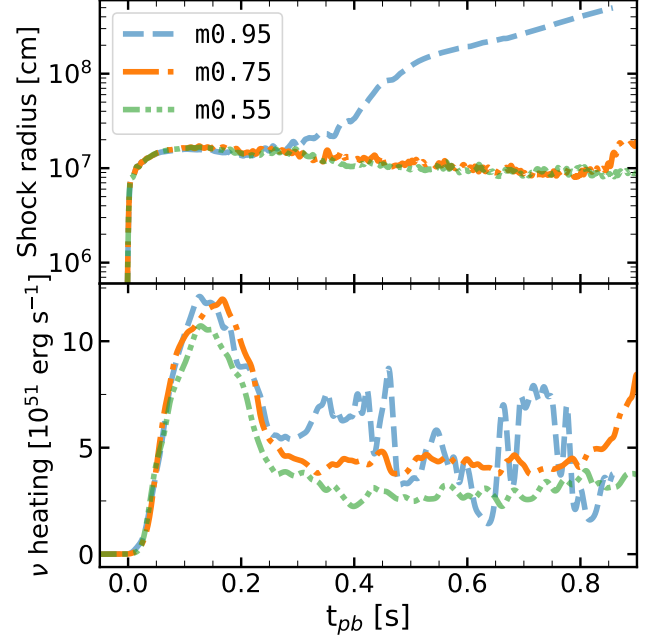


Figure 1. Evolution of the mean shock radius (*top panel*) and the neutrino heating (*bottom panel*). Shock revival occurs for $m0.95$ at ~ 300 ms post-bounce, and for $m0.75$ at ~ 900 ms post-bounce, whereas the simulation with the lowest value of the effective mass parameter does not explode in the simulated time. This is generally consistent with the increased electron-type neutrino luminosity and mean energies and therefore neutrino heating for the simulations with the higher effective mass, making conditions more favorable for shock revival.

3. RESULTS

In this section, we describe the main results of our study. We first present results for three axisymmetric CCSNe simulations that show how the effective mass affects the PNS evolution and GW signal for the non-rotating $20 M_{\odot}$ progenitor of Woosley & Heger (2007). Then we explore the effect of two rotation rates, $\Omega_0 = 1$ and 2 rad s^{-1} , in the GW signal considering the two extreme cases studied for the effective mass. Finally, as a matter of interest and to reaffirm the findings of Schneider et al. (2019), we explore the impact of the isoscalar incompressibility, K_{sat} , within its current experimental constraint. Recall that we label the simulations following the convention in Table 2. Following this, we explore the spatial origin of the GWs in our models and the power gap. All of the GW wave strains reported in this work are available at <https://doi.org/10.5281/zenodo.4973546>.

3.1. Effective Mass

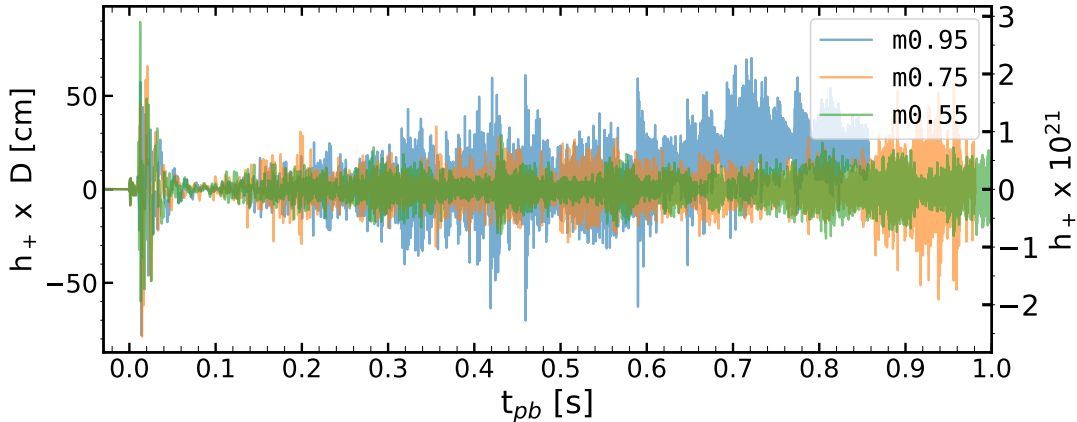


Figure 2. Gravitational wave signals for models varying in the effective mass parameter as measured from an arbitrary distance (left axis) and from 10 kpc (right axis), assuming that the observers are standing in the equatorial plane of the source. Generally, the GW amplitude increases with a larger value of the effective mass parameter. Around 0.6 s, the signal for the $m0.95$ model undergoes a shift in the positive direction due to a prolate shape of the shock during explosion.

When investigating the effective mass dependence of GWs for non-rotating progenitors, the three simulations we compare are carried out for a minimum of 860 ms post-bounce. Each stellar core collapses until the EOS stiffens and bounce occurs (at 318.5 ± 0.1 ms after the onset of the simulation), followed by the formation and outward propagation of the shock wave that initially stalls at ~ 170 km at ~ 100 ms after bounce. The top panel of Figure 1 shows the evolution of the mean shock radius. Shock revival occurs for $m0.95$ at ~ 300 ms post-bounce, and for $m0.75$ at ~ 900 ms post-bounce, whereas the simulation with the lowest value of the effective mass parameter, $m0.55$, does not explode in the simulated time. This is consistent with the generally increasing neutrino heating expected for higher effective masses (bottom panel of Figure 1), making conditions more favorable for shock runaway (Janka 2017; Yasin et al. 2020; Schneider et al. 2019). The difference in neutrino heating between the simulations is a reflection of the neutrino luminosity and neutrino mean energy, both of which increase with the effective mass. We remark that this trend is seen for all neutrino/anti-neutrino species with eventual deviations related to the times of explosion.

Neutrino heating does not only provide the shock with thermal support and aid in shock revival, it also drives turbulence and convection in the gain region (Couch & Ott 2015) that imprints on the gravitational waves. Figure 2 shows the gravitational wave signals. While we note a strong signal at epochs $\lesssim 70$ ms that is typically attributed to prompt convection (Murphy et al. 2009), our analysis focuses on epochs after 0.1 s when the quiescent phase has ended and the excitation of PNS oscil-

lations begins. During this phase, such PNS oscillations strongly dominate the GW signal. The amplitude of the gravitational waves increases with higher effective mass. We attribute this, at least in part, to the increasingly (neutrino driven) “violent” gain region in simulations with higher effective mass, correlating with the amplitude of the PNS oscillations via accretion plumes striking the convectively stable layer below (Murphy et al. 2009; Yakunin et al. 2015). Radice et al. (2019) shows, albeit in 3D, that the energy radiated in GWs is proportional to the amount of turbulent energy accreted by the PNS. Here, we note (but do not show) that the total energy radiated increases with the effective mass throughout all evolutionary stages above 0.1 s. It is worth noting that the development of an explosion, as long as there is sustained accretion, can lead to GWs with an amplitude at a level higher than it would have been without an explosion (Radice et al. 2019), therefore, the high GW amplitude seen in $m0.95$, and to some extent in $m0.75$, after the onset of explosion can be in part attributed with this as well. We return with an in-depth analysis and discussion regarding the source of the GWs in § 3.4.

As seen in previous studies (e.g. Murphy et al. 2009; Yakunin et al. 2015), we observe a prolate shape of the shock for the $m0.95$ model which is reflected in the GW signal by a shift in the positive direction at ~ 0.6 s.

In Figure 3, we show the spectrograms where the typical, dominant PNS oscillation GW signal starts at ~ 0.1 s and increases in frequency as the PNS cools and contracts. In all three spectrograms, we note a particular region that appears to lack emission, located at roughly constant frequency (~ 1.2 kHz) throughout the

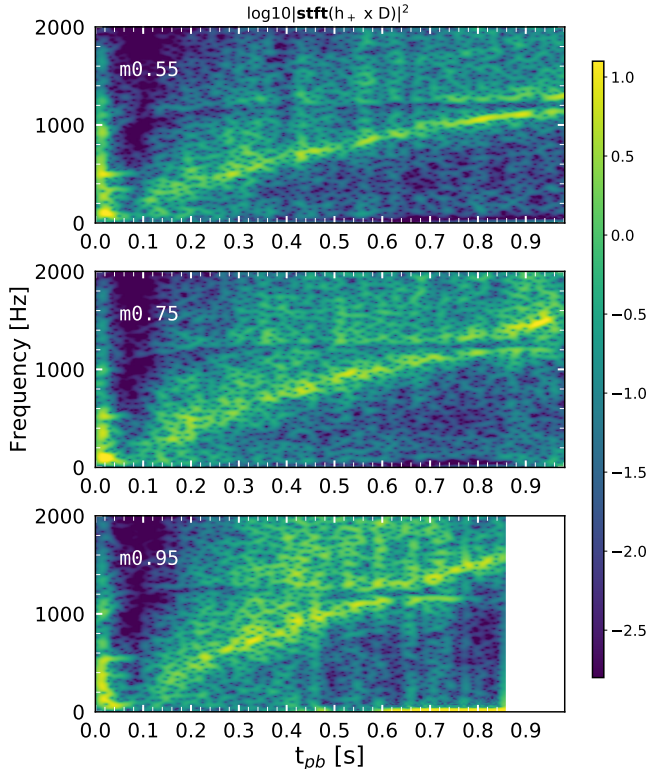


Figure 3. Logarithmic spectrograms of the gravitational wave signal for the three simulations varying in the effective mass. For a direct comparison, they are normalized across their global maximum above 100 ms. There are three distinct features in the spectrograms: (1) strong emission over a large range of frequencies $\lesssim 70$ ms typically attributed to prompt convection, (2) a narrow band of high power that increases in frequency with time, the dominant PNS oscillation frequency, and (3) a region located at approximately constant frequency (~ 1.2 kHz) that appears to lack emission, the “power gap” which we explore in §3.5.

simulation time. Morozova et al. (2018) were the first to address this “power gap”, which they could not attribute to a numerical artifact, and, thus, do not rule out a physical origin. As the dominant oscillation mode evolves towards the gap region from below, an interaction appears to take place with another mode above the power gap, consistent with the avoided-crossing description in Morozova et al. (2018); Sotani & Takiwaki (2020), resulting in the lower frequency mode flattening out in frequency and dropping in amplitude, while the other higher frequency mode rises in frequency and amplitude. The crossing between modes occur at roughly ~ 650 ms, ~ 850 ms, and ~ 1000 ms for the m0.95, m0.75, and m0.55 simulations, respectively. We report our further exploration of the power gap in §3.5.

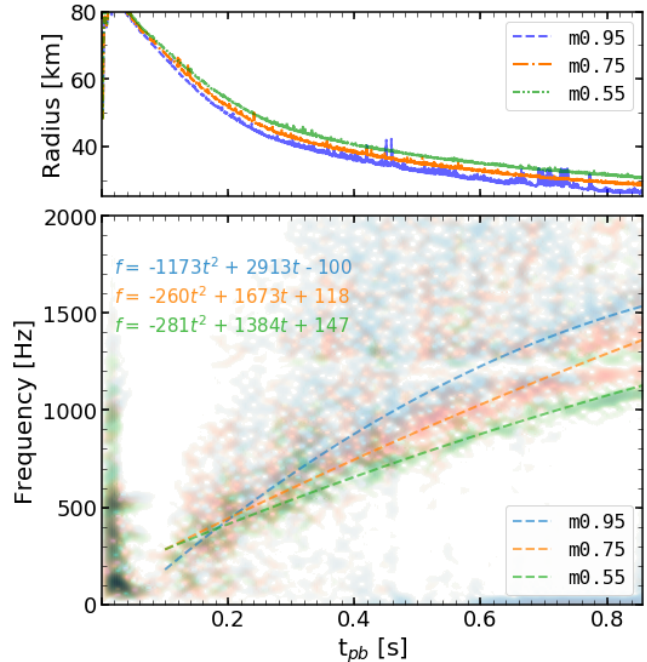


Figure 4. *Top panel:* PNS radius defined as the maximum radius where the density is at least 10^{11} g cm $^{-3}$. *Bottom panel:* Overlaid spectrograms of the three models varying in effective mass and overplotted with second order polynomial fits to the frequency points of most power. The window over which the fit is made is from 0.1 s to the end of the simulation time. The polynomial coefficients are shown in the top left corner.

We show in Figure 4 the radius of the PNSs (top panel) and the three spectrograms overlaid on one another (bottom panel). We define the PNS radius as the maximum distance to where the density is 10^{11} g cm $^{-3}$ which leads to sporadic jumps in the evolution profile of the early-exploding run, m0.95. The dashed lines in the spectrogram plot are quadratic fits of the form $At^2 + Bt + C$ to the collection of frequency points of most power (one extracted per STFT time-step of 3.6 ms). The PNS radius and the frequency of the dominant oscillation mode are clearly effective mass dependent. It has been realized through asteroseismology studies (e.g. Morozova et al. 2018; Torres-Forné et al. 2019a) and works using semianalytical fits to the dominant frequency (e.g. Müller et al. 2013; Pan et al. 2018; Pajkos et al. 2019), that the mass and radius are the primary determinants of the dominant PNS oscillation frequency. The masses of the accreting PNSs remain equal between our models until ~ 0.5 s after bounce and differ by at most 4% by the end of run m0.95 (at $t_{pb} = 860$ ms) due to explosion, at which point the radii differ by ~ 15 % between our two extreme cases. Hence, the radius holds

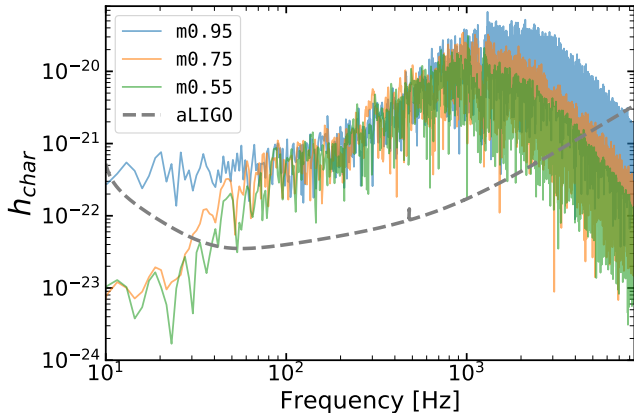


Figure 5. Characteristic strain as a function of frequency, assuming a distance to the source of 10 kpc. This is calculated between 100–860 ms post-bounce. The peak frequency and its corresponding strain increases as the value of the effective mass increases. The grey dashed line represents the sensitivity bounds of Advanced LIGO (Barsotti et al. 2018), indicating potential of detecting gravitational wave signals from a Galactic CCSNe of similar physical properties as these models.

the dominant role in setting the frequency and accounts for the $\sim 36\%$ difference in frequency at 860 ms between run m0.55 and m0.95. As expected due to the role of the effective mass on the thermal properties outlined in Schneider et al. (2019) and mentioned above, we find that a higher value of the effective mass parameter m^* yields a more compact PNS, producing a higher oscillation frequency.

Figure 5 shows the characteristic strain, h_{char} (Eq. 7) where we assume a distance of 10 kpc to the source. The frequency corresponding to the largest h_{char} , the so called peak frequency, is shifted to higher frequencies and higher power when increasing the effective mass, *i.e.*, when increasing the PNS compactness. The peak frequencies are located around 1-2 kHz, indicating that these amplitudes are due to the PNS oscillations. The power gap near 1.2 kHz is also clearly seen in this plot. Furthermore, because the peak frequency rises slower in the m0.55 run and the window over which h_{char} is calculated is limited to the maximum common run time, $t_{\text{pb}} = 860$ ms, the characteristic strain for this run above the power gap is lower than below the gap. This is not the case for the m0.75 and m0.95 runs, where the peak frequency crosses the power gap $\simeq 200$ ms earlier.

Another feature we observe is a small shoulder of excess emission around ~ 100 Hz which may be attributed to the standing accretion shock instability (SASI) or more generally, neutrino-driven convection and turbulent flows in the gain region, where the GW radiation

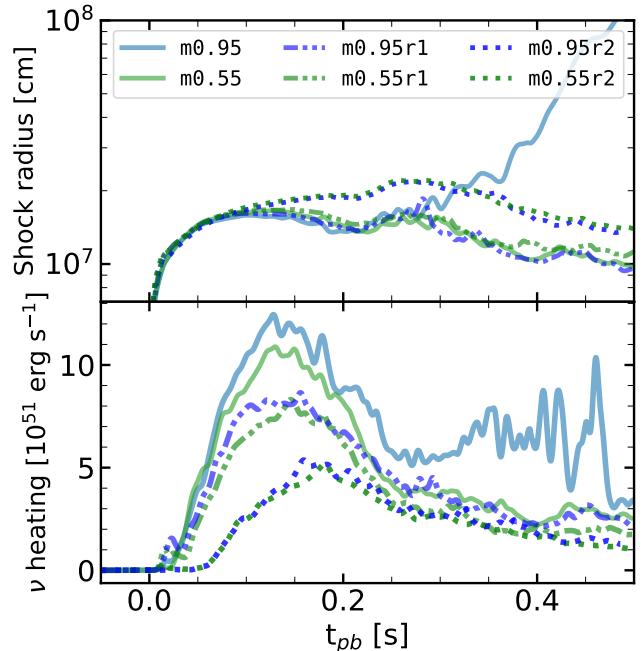


Figure 6. *Top panel:* Evolution of the mean shock radius comparing non-rotating models (solid lines), $\Omega_0 = 1 \text{ rad s}^{-1}$ rotation (dashed-dotted lines), and $\Omega_0 = 2 \text{ rad s}^{-1}$ rotation (dotted lines) for the $m^* = 0.95$ (blue) and the $m^* = 0.55$ (green) EOSs. When rotation is included, no shock revivals occur during the ~ 0.5 s simulation time. *Bottom panel:* Neutrino heating. Due to centrifugal support, rotating progenitors produce less compact PNSs, releasing less gravitational binding energy in the form of neutrinos and impacting the neutrino heating.

is typically emitted at such low frequencies (e.g. Cerdá-Durán et al. 2013; Pan et al. 2018; Pajkos et al. 2019). For the m0.95 run there is also an excess emission at frequencies $\lesssim 100$ Hz due to the asymmetric explosion.

The grey dashed line in Figure 5 represents a sensitivity curve of Advanced LIGO (Barsotti et al. 2018). The frequency and amplitude ranges are well within the bounds of the sensitivity curve. Caution should be taken when concluding their detectability since 2D simulations typically overpredict the signal strength compared to 3D simulations. Several 3D studies report on amplitudes decreasing by a factor between 10 – 20 in their 2D/3D comparisons (Andresen et al. 2017; O’Connor & Couch 2018b; Mezzacappa et al. 2020), which would make a detection at 10 kpc more marginal, for example see Szczepanczyk et al. (2021).

3.2. EOS and Rotation

For our models with the highest and lowest values of the effective mass parameter, we run additional simulations using rotation profiles with central angular speeds

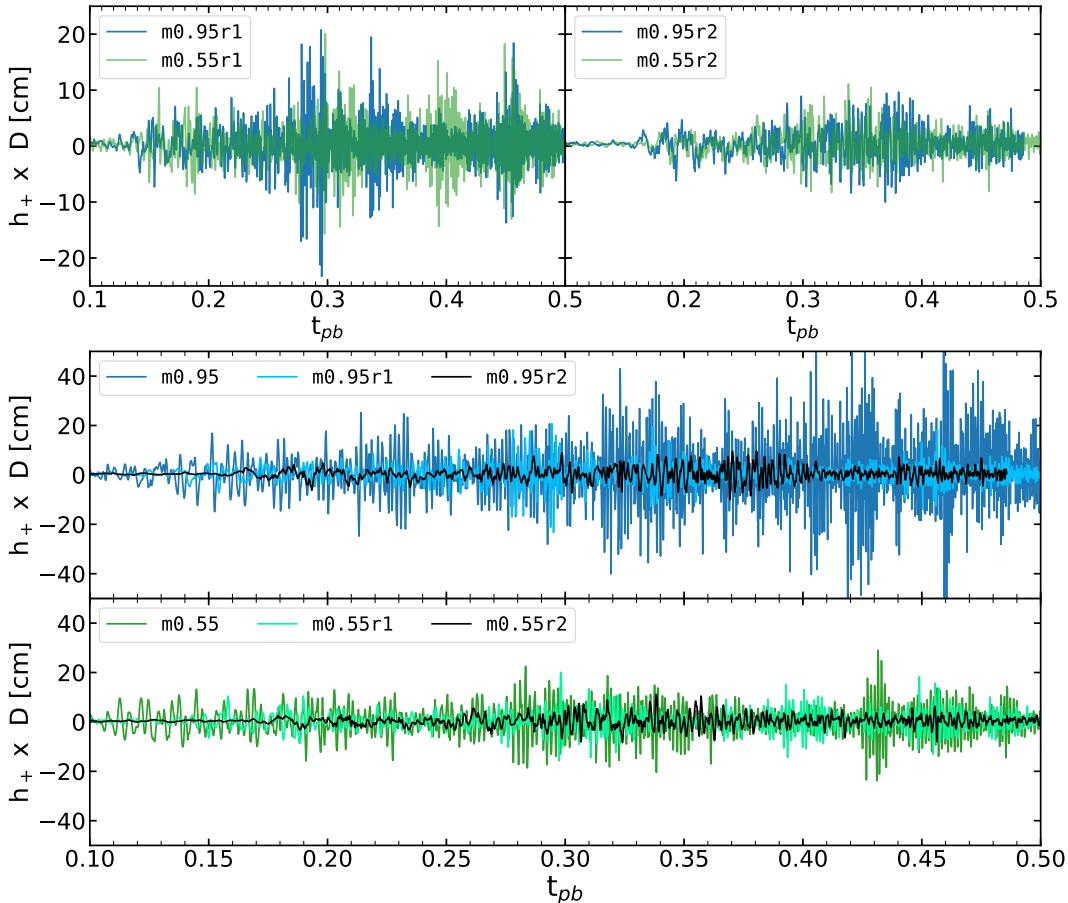


Figure 7. GW signal for the models varying in both effective mass and rotation rate. *Top left panel:* models with $\Omega_0 = 1 \text{ rad s}^{-1}$. *Top right panel:* models with $\Omega_0 = 2 \text{ rad s}^{-1}$. *Middle panel:* the $m^* = 0.95$ models. *Bottom panel:* the $m^* = 0.55$ models. The two bottom panels emphasize how the signal becomes increasingly muted with higher rotation rate. The two panels on top show that the signal is muted to similar amplitude for equal rotation rates. Thus, the effective mass dependence of the GW amplitude is washed out by the somewhat centrifugally stabilized gain region.

of 1 rad s^{-1} and 2 rad s^{-1} at the onset of collapse (see Eq. 1). Figure 6 shows the mean shock radius (top panel) and the neutrino heating (bottom panel). In contrast to the non-rotating $m0.95$ simulation, no shock revivals occur for either $m0.95r1$ nor $m0.95r2$ during their $\sim 0.5 \text{ s}$ simulation time.

Due to centrifugal support, matter does not settle as deeply in the gravitational potential, releasing less gravitational binding energy during core collapse. This results in lower neutrino luminosity and slower contraction of the PNS (Westernacher-Schneider et al. 2019; Summa et al. 2018). When we increase the rotation rate, we observe a significant non-linear decrease of the neutrino/anti-neutrino luminosities (as well as mean energies) which is reflected in the neutrino heating (Figure 6). Other processes may factor into the observed

heating also: for the most rapidly rotating models, the centrifugally supported shocks are located at a large radius, increasing the region where neutrinos may deposit energy. On the other hand, when including rotation, convection is inhibited due to a positive angular momentum gradient which is known to result in less prominent neutrino heating. (Murphy et al. 2013).

Figure 7 shows the GW signal for the models varying in both the effective mass and rotation rate. Expectedly (e.g. Pajkos et al. 2019), the two bottom panels illustrate how the signal becomes increasingly muted with a higher rotation rate. As demonstrated by the two neighboring panels on top, and contrary to the non-rotating simulations, we do not find any effective mass dependence of the GW amplitude for our simulations

that include rotation. This is of special note for the 1 rad s^{-1} models as they still exhibit an effective mass dependence in neutrino heating. The centrifugal support stabilizes the gain region to the extent that the different amounts of neutrino heating has little to no impact on the GW amplitude. Furthermore, it takes longer for the convection instabilities in the 2 rad s^{-1} models to become fully non-linear in the gain region and thus these simulations exhibit an extended quiescent phase until $\sim 150 - 170 \text{ ms}$. Since these simulations are axisymmetric, the suppression of GW emission we see here due to rotation could be overestimated as compared to 3D. Furthermore, for sufficiently high rotation rates one expects non-axisymmetric instabilities give rise to potentially strong GWs (Scheidegger et al. 2010; Andresen et al. 2019; Takiwaki & Kotake 2018).

Figure 8 shows the PNS radii (top panel) as well as the polynomial fits to the frequency points of most power (bottom panel). Correlated with the radius (that increases non-linearly with higher rotation rate), the frequency of the dominant PNS oscillation mode decreases with increasing rotation. The effective mass dependence of this mode is still clear for the 1 rad s^{-1} simulations, with rotation at this level only reducing the peak frequency by $\sim 10\%$ from the respective non-rotating counterparts. For the 2 rad s^{-1} models, due to the relatively little PNS excitation (and late onset thereof, see Figure 7), the frequency distribution of power is much more broad and at a lower level. Nevertheless, using a linear fit to the frequency points of most power for these rapidly rotating models (see the bottom panel of Figure 8), we see a further reduction in the peak frequency and remark that the rapid rotation washes out any discernible frequency dependence that the slightly different PNS radii of the fast rotating simulations would cause.

3.3. Incompressibility

The results above highlight how the compactness of the PNS at the time of formation as well as its cooling rate are the underlying factors of the GW signatures (under otherwise similar conditions). Indirectly so for the GW amplitude via the neutrino emission, and a more so direct correspondence between the PNS radius and the peak GW emission frequency.

For the simulations where we investigate the effect of the incompressibility modulus, the PNS masses and radii are nearly identical across the models during their $\sim 0.6 \text{ s}$ simulation time. This agrees the spherically symmetric results of Schneider et al. (2019). Expectedly, we see no systematic differences in the GW signatures between the three models, and any minor differences are likely stochastic. Figure 9 shows the characteristic strain

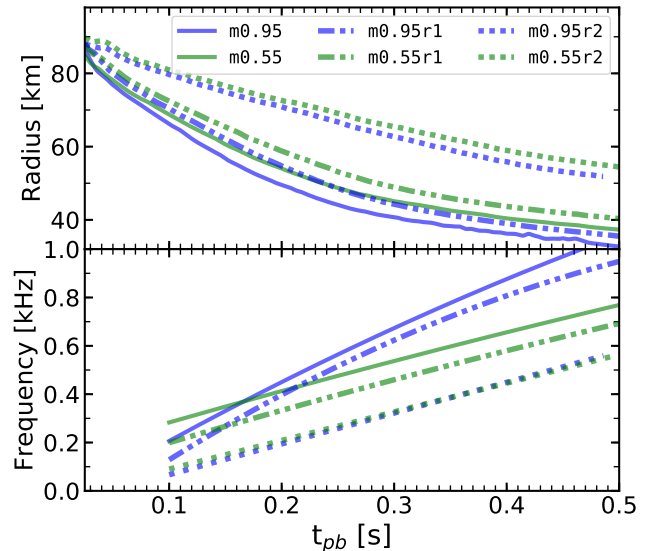


Figure 8. The PNS radius (*top panel*) for the models varying in both effective mass and rotation rate, as well as the polynomial fits to the frequency points of most power (*bottom panel*). These frequencies are extracted from the spectrograms (one per time-step of 3.6 ms) and we only use frequencies above 120 Hz . For the 2 rad s^{-1} models, we use a linear fit due to a less well-defined dominant mode in the spectrogram (see text). The effective mass dependence of the dominant PNS oscillation frequency is still seen for the 1 rad s^{-1} models, but not the 2 rad s^{-1} models.

as a function of frequency, which reflects the similarity in both amplitude and frequency between the three simulations. We note that the decrease in GW emission in the 1.0 to 1.2 kHz range is even more evident in Figure 9 now that the characteristic strains of the simulations h_{char} overlap. We discuss the incompressibility dependence of the gap further in §3.5.

3.4. Source of the GWs

In a typical PNS there are two convectively stable regions, one in the inner core and one that composes the outer shell of the PNS that faces the turbulent post-shock region. According to canonical wave theory Handler (2013) (also see Gossan et al. (2020) for a direct application in CCSNe), apart from oscillatory p-modes (where pressure acts as restoring force) at high frequency, these stable regions may also house g-modes at lower frequencies (where buoyancy acts as restoring force). These excitations may emit GWs at select eigenmode frequencies when excited. Often, a buoyantly unstable region separates the core and the outer shell, the PNS convection zone. In 2D, many groups have attributed their GW signal to g-modes from the outer

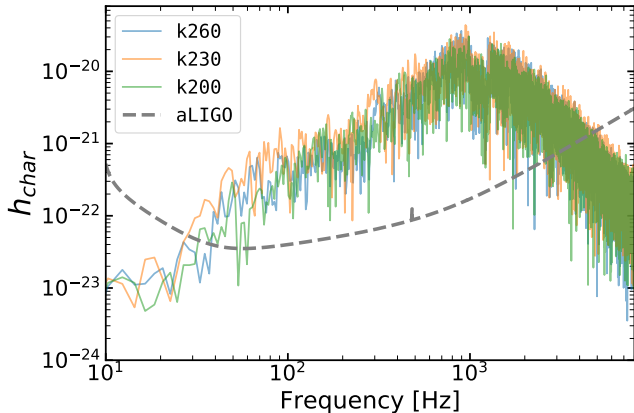


Figure 9. Characteristic strain as a function of frequency for the models varying in the incompressibility modulus, K_{sat} , assuming a 10 kpc distance to the source. This is calculated between 100 – 580 ms post-bounce. The grey dashed line represents the sensitivity bounds of Advanced LIGO (Bartotti et al. 2018). There is little to no dependence of the GW signal on the incompressibility modulus.

shell (Cerdá-Durán et al. 2013; Müller et al. 2013; Pan et al. 2018). A viable perturbing mechanism is accretion plumes impinging onto the PNS from the violent gain region above (Murphy et al. 2009), also recognized in 3D (O’Connor & Couch 2018b; Radice et al. 2019; Powell & Müller 2019).

Adding to the possibilities of strong GW sources, Mezzacappa et al. (2020) conclude that after a few 100s of ms, PNS convection takes over as the dominant source of GW emission in their 3D study. Andresen et al. (2017) report that the dominant source of emission in their 3D runs originates from the bottom end of the convectively stable surface layer, driven by convective overshoot from the convection zone below rather than by accretion from above, and further show the same scenario for a 2D counterpart to a 3D run. It should also be mentioned that PNS convection has previously been recognized as a GW source and as a possible g-mode excitation mechanism in 2D (Murphy et al. 2009; Marek et al. 2009; Müller et al. 2013), and in 3D (Müller et al. 2012), although not established as a dominant source pre-explosion. Furthermore, Torres-Forné et al. (2019b) (in 2D) point towards the stable inner core as the region responsible for the dominant emission in their study, and support the hypothesis that the dominant emission is always a g-mode (Torres-Forné et al. 2019a). For Morozova et al. (2018) and Sotani & Takiwaki (2020) in 2D, and for Radice et al. (2019) in 3D, their dominant source of emission after roughly 0.4 s stems from the fundamental quadrupolar mode, having transitioned from a g-mode.

It is possible that the dominant GW emission is strongly model dependent and that the scenery of strong GW emission in CCSNe is as rich as the literature suggests. It is further possible that the situation is more generic and a stronger consensus will emerge as PNS asteroseismology techniques and classification methods become even more sophisticated and widely used. However, only a couple (Andresen et al. 2017; Mezzacappa et al. 2020) spatially decompose their GW signals from the actual simulation. Thus, to shed light on the excitation mechanism, we encourage the combination of self-consistent perturbation analysis and spatially resolving the emission. In this work, we refrain from firmly diagnosing our dominant emission with a particular mode, we leave this to future work. Instead, we attempt to localize the source of the GWs in our simulations while simultaneously highlighting two analytical procedures, hoping to provide value to future studies in unveiling the mechanism and source of GWs:

(1) In Appendix A we remark that caution needs to be taken when calculating the spatial distribution of GWs since the often-used analytic expression for the first time derivative of the quadrupole moment (Eq. 4 in Cartesian and Eq. A5 in spherical coordinates) neglects a surface term when considering only a portion of the PNS. This term, of course, vanishes when calculating the GW emission from the whole star. In that appendix we show how, when instead numerically taking two time derivatives of the quadrupole moment itself, the apparent emission region changes. In particular, emission that was previously seemingly from the convection zone, where the surface terms are largest, decreases.

(2) In Appendix B we highlight that the location where the energy density associated with a particular mode (Torres-Forné et al. 2018; Morozova et al. 2018; Torres-Forné et al. 2019b; Sotani & Takiwaki 2020) is most concentrated, does not necessarily overlap with the region emitting the largest contribution of GWs due to the excitation of that mode. This is for two reasons, (a) because significantly more mass is located further out at larger radii, even though the energy density is lower and (b) the added lever arm of the radius (squared) in the quadrupole moment. As a consequence of this analysis, we show that the radial profile of the GW emission at any particular frequency, computed from either a perturbation analysis or dynamically from the simulation agree remarkably well in the PNS itself.

With these in mind, we attempt to localize the source of the GW emission in our 2D simulations and place the results in the context of the literature. In Figure 10, we show the spatial distribution of the radial velocity (top panels) and radial profiles of the GW spectrogram (bot-

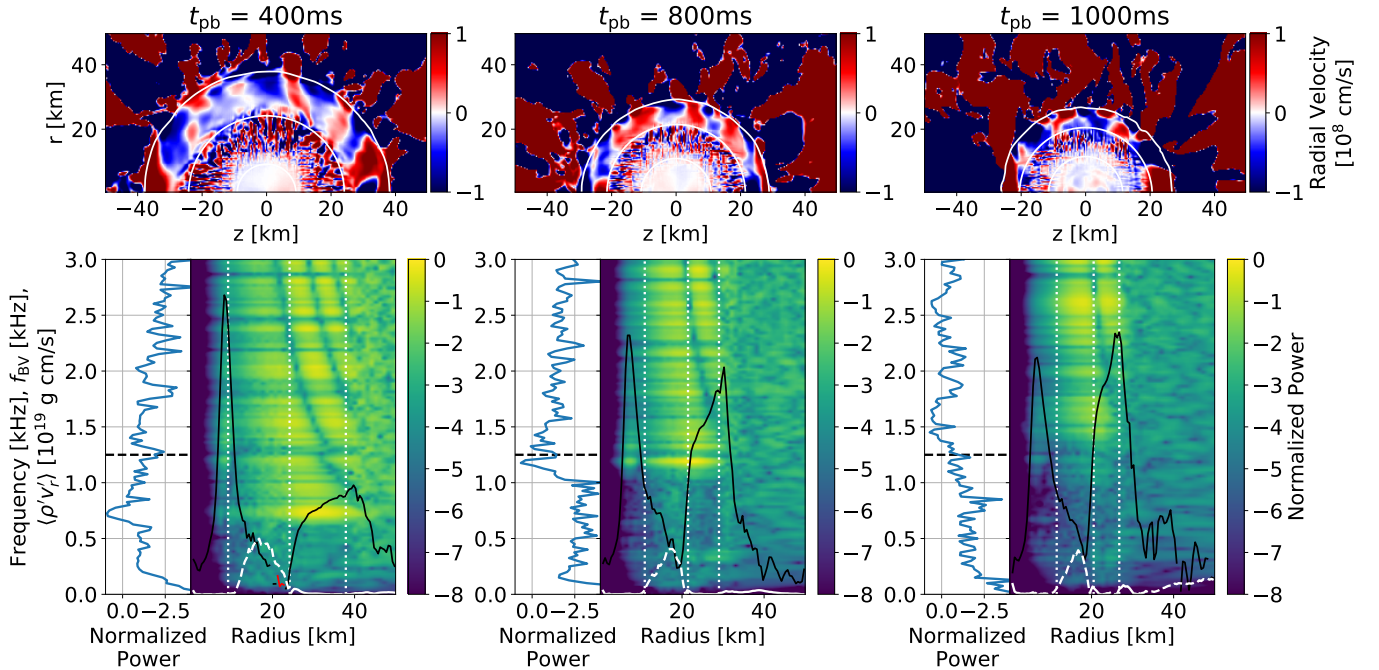


Figure 10. Spatial distributions of the radial velocity (*top panels*) where red (blue) colors denote positive (negative) radial velocities, as well as radial profiles of the GW spectrogram (*bottom panels*) at times $t = 400$ ms (left), $t = 800$ ms (middle), and $t = 1000$ ms (right) after bounce for model $m0.75$. In contours (top) and vertical dashed lines (bottom) we denote the location of $\rho = 10^{11}$, 10^{13} , and 2×10^{14} g cm^{-3} . These roughly divide the PNS core, PNS convection zone, the convectively-stable PNS surface layer, and the gain region (and beyond). To the left of each spectrogram profile we show the projected power spectral density, with an explicit dashed line at 1250 Hz to highlight the location of the power gap. On each of the spectrogram profiles we show the Brunt-Väisälä frequency (Eq. 10) in black (red denotes negative values of f_{BV}^2) and the turbulent energy flux (Eq. 9) in white (dashed denotes negative values).

tom panels) for $t = 400$ ms (left), $t = 800$ ms (middle), and $t = 1000$ ms (right) post-bounce for our baseline simulation, $m0.75$. The GW signal in these spectra are calculated in the post-processing of high cadence data by taking two numerical time derivatives of the contribution to the zz component of the quadrupole moment (i.e. Eq. 3) contained in each spherical shell (and multiplying with the constants outside the double derivative in Eq. 5). We note this is different than using a radially decomposed Eq. 4 and taking one additional time derivative, we refer the reader to Appendix A for the important details. We obtain the frequency dependence by multiplying this radially-decomposed GW signal with a 40 ms Hann-window centered at each time specified above, and finally Fourier transform it. To the left of each spectrogram profile we show the normalized projected power spectral density. We note that both the profile and projection are logarithmic. In each spectrogram profile we also plot the turbulent energy flux (white solid lines for positive values and dashed for negative values). Similar to Eq. 15 – 17 in Andersen et al.

(2017), the turbulent energy flux, f_m , is calculated via,

$$f_m = \langle \rho' v_r' \rangle, \quad (9)$$

where angled brackets denote an angular average, ρ denotes mass density, and v_r is the radial velocity of the fluid. Here, the primed quantities are the deviations from the angle average, e.g. $\rho' = \rho - \langle \rho \rangle$. To reduce the stochastic noise of f_m in our 2D simulations, the curves in Figure 10 are an average of all the turbulent energy flux profiles obtained over the 40 ms window. We also include the Brunt-Väisälä frequency (black lines) following Mezzacappa et al. (2020),

$$f_{BV}^2 = -\frac{\partial \phi / \partial r}{(2\pi)^2 \rho} \left(\frac{\partial \rho}{\partial s} \Big|_{P, Y_{lep}} \frac{ds}{dr} + \frac{\partial \rho}{\partial Y_{lep}} \Big|_{P, s} \frac{dY_{lep}}{dr} \right), \quad (10)$$

where $Y_{lep} = Y_e + Y_\nu$, and both P and s include contributions from the neutrinos as well. For these neutrino contributions, we assume a thermal distribution of neutrinos at densities higher than $\sim \rho = 10^{12}$ g cm^{-3} (Kaplan et al. 2014). While in principle the convective region should have negative f_{BV}^2 , we only see this for the outer part of the convection zone for the $t = 400$ ms profile,

and therefore we rely on the turbulent energy flux to define the convection zone. For each of the three times, we mark the location of $\rho = 10^{11}$, 10^{13} , and $2 \times 10^{14} \text{ g cm}^{-3}$ with dashed vertical lines in the spectrograms and as contours in the radial velocity plots.

In Figure 10, the convective region is traced very well by the width of the negative part of the turbulent energy flux profile. Inside the convection zone, heavier fluid is advected downwards while fluid that is lighter than average rises upwards. The turbulent energy flux will thus always be negative in the convective layer. The reverse is true in the overshoot layer above the PNS convection zone as the overshoot plumes are more dense than the local average, explaining the small positive peak in the turbulent energy flux just above the convection zone in Figure 10. Hence, as seen in the figure, the radius corresponding to $\rho = 2 \times 10^{14}$, 10^{13} , and $10^{11} \text{ g cm}^{-3}$, roughly divides the PNS core, the PNS convection zone, the convectively-stable PNS surface layer, and the gain region (and beyond). This is further highlighted by the density contours in the radial velocity plots in the top panel of Figure 10 where funnels of fast-moving matter in opposite directions are seen between $\rho = 10^{13} \text{ g cm}^{-3}$ and $\rho = 2 \times 10^{14} \text{ g cm}^{-3}$, namely convection sustained and driven by continued neutrino diffusion out of the core and the maintenance of the lepton gradients. For completeness, we show in Figure 11 properties of the PNS convection zone over the course of the simulations for each non-rotating simulation. Following the PNS radius trend in Figure 4, the PNS convection zone is located at a larger radius for simulations with a lower effective mass. While the smallest (largest) in volume, the m0.95 (m0.55) simulation shows the largest (smallest) PNS convection zone mass and kinetic energy at early times ($t \lesssim 300 \text{ ms}$). At late times, the mass contained in the convection zone levels out and the ordering inverts, with the m0.95 simulation having less mass than the others. This may be due to the explosion in the m0.95 simulation. At the level explored here, K_{sat} does not impact any of the PNS convection properties.

Regarding the source of the GWs and the radially decomposed spectrograms in Figure 10, resolving a precise location in the star where the emission occurs is difficult. The emission region is extended, which is supported by the results shown in Appendix B, where we show, for these select times, the radial profile of the GW emission compared to the predictions from a perturbation analysis. However, the figure provides a strong indication that the dominant emission in our simulations stems from the convectively stable surface layer, with a tendency towards the bottom end of this layer, the convective overshoot region. Characteristic of

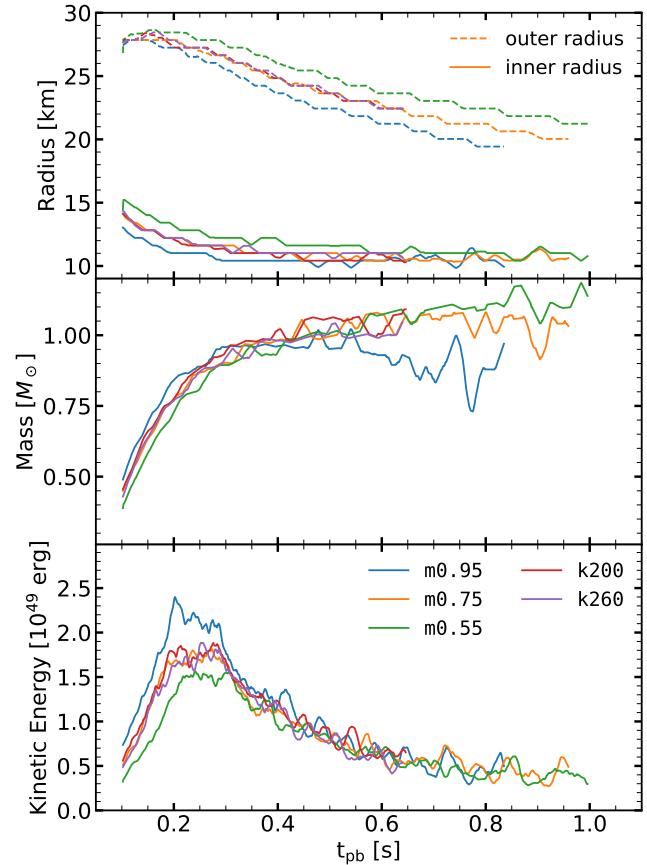


Figure 11. *Top panel:* Radial boundaries for the PNS convection zone as defined by the location where the turbulent flux is $f_m = 0.1 \times f_m^{\text{min}}$ (inner) and $f_m = 0$ (outer). *Middle panel:* PNS convection zone mass. *Bottom panel:* PNS convection zone total kinetic energy. Data are smoothed over 20 ms.

g-modes, the $\rho = 10^{13} \text{ g cm}^{-3}$ line, which closely traces the location of the overshoot region, crosses the Brunt-Väisälä frequency in close proximity to the dominant emission region, especially at $t = 800 \text{ ms}$ (middle), and $t = 1000 \text{ ms}$ (right). While our analysis suggests that the dominant source of GW emission does not stem from the convection zone itself, we cannot rule out PNS convection as a forcing mechanism that accounts for a substantial fraction of the GWs generated. In fact, we think this is plausible and supports the findings of [Andresen et al. \(2017\)](#) who also find significant emission in the PNS convective overshoot region. On the other hand, considering the correlation we see between the GW amplitudes and the neutrino heating (§3.1 and §3.2), as well as the non-correlation with the total PNS convection layer kinetic energy seen in Figure 11, we neither rule out accretion plumes as a strong excitation mechanism. Furthermore, via entropy field plots we

observe clear funnels of low-entropy matter (from the gain region) striking the PNS at times coinciding with some of the largest amplitude spikes in the GW signal. Perhaps these simulations serves as an example where both mechanisms are at work.

Several groups report on GW amplitudes decreasing by a factor 10–20 when going from 2D to 3D (Andresen et al. 2017; O’Connor & Couch 2018b; Mezzacappa et al. 2020). This is generally expected since the axisymmetric assumption leads to an artificial enhancement of coherent motion. Andresen et al. (2017) gather the contributions to the GW signal from different regions, such as the convection zone plus its overshoot layer (region A in their paper) and the PNS surface layer (region B in their paper). They report on a suppression of the GW signal by a factor of ~ 10 in region A when going from 2D to 3D, and a higher such factor in region B. Andresen et al. (2017) discuss why a higher suppression of GWs excited by accretion plumes, compared to overshoot from below, is expected when going from 2D to 3D. In 2D, turbulence structures cascade in reverse (Xiao et al. 2009) and the Kelvin-Helmholtz instability is suppressed at the edge of supersonic downflows (Müller 2015), this may result in artificially high accumulation of the turbulent energy on large scales, and higher downflow velocities onto the PNS. Furthermore, Andresen et al. (2017) demonstrate that in 2D, the frequency range of the chaotic turbulent downflows from the gain region may have a stronger overlap with the natural g-mode frequency, such that the accretion mechanism may produce more resonant excitation in 2D compared to 3D. Speculatively then, if both the convective overshoot and the accretion mechanisms drive the GWs in our simulations, and with these effects taken into account, 3D counterparts to our models may have convective overshoot as the main forcing of PNS oscillations, however, based in Appendix B, we do not expect the radial distributions to change dramatically.

3.5. Origin of the Power Gap

We end our results section by exploring the power gap present in all of our simulations. We show the evolution of the characteristic strain for the m0.75 run in the top panel of Figure 12, where we have sequentially windowed 200 ms of the GW signal centered at the epoch we specify on the right hand side. For a direct comparison, each but the first strain is shifted vertically using even multiplication factors on a logarithmic scale. The strains are plotted in color, with smoothed versions in black. This figure provides yet another perspective of the drift of

the peak frequency corresponding to the dominant PNS oscillation mode which goes from ~ 550 Hz at 280 ms to ~ 1450 Hz at 880 ms. The power gap, which we mark by crosses at the local minima of the black lines, is located around 1.2 kHz and is particularly easy to see between 0.6–0.9 s when modes are excited both above and below the gap. In the bottom panel, we plot the location of the minimum over many time steps for the three models varying in effective mass and for the three models varying in incompressibility modulus. Recall that m0.75 and k230 are the same, and our baseline simulation.

Addressing the models varying only in the effective mass first, before ~ 0.3 s, the gap locations are ordered in frequency with the value of the effective mass. For m0.55 and m0.75, which share the same general gap evolution, the frequency of the gap increases until it flattens out around ~ 0.4 s and stays roughly constant thereafter. The gap evolution of the m0.95 simulation differs from the others since its frequency decreases with time.

The evolution of the gap does not appear to change when varying the incompressibility modulus. However the quantitative value of the gap frequency does. It is located at lower frequencies for progressively higher values of K_{sat} . Recall the k200 and k260 simulations are only carried out until ~ 600 ms after bounce.

Morozova et al. (2018) speculate that one may view the PNS as a coupled system of the inner core and the outer convectively stable shell, mediated by the PNS convection zone, such that the power gap may originate via a repelling interaction between a trapped PNS core mode and a surface layer mode. Their perturbation analysis roughly reproduces the morphology of the gap when plotting the frequency of modes after having moved the outer boundary to the core surface (their Figure 8).

The different gap frequencies (bottom panel of Figure 12) in our study further hints towards an involvement of the inner core in producing the power gap. The incompressibility modulus has only a significant effect in the core, where the density is sufficiently high and the thermal component of the EOS is less dominant (Schneider et al. 2019). Recall that the PNS radius defined at $\rho = 10^{11} \text{ g cm}^{-3}$ and the PNS convection zone properties, which reflects the structure between $\sim 10^{13} - 10^{14} \text{ g cm}^{-3}$, remain equal between the models varying in incompressibility modulus. Thus, the outer structure of the PNS alone is likely not the cause of the gap, nor sets the frequency. However this inner core structure may. Varying the incompressibility (effective mass) above and below baseline changes the central density by $\sim 4\%$ ($\sim 12\%$). Furthermore, the central density and the gap frequency share the same ordering

between all the models. That is, the higher the central density, the higher the frequency of the gap. The $m0.95$ run is the only deviation to this trend due of its deviation in gap morphology.

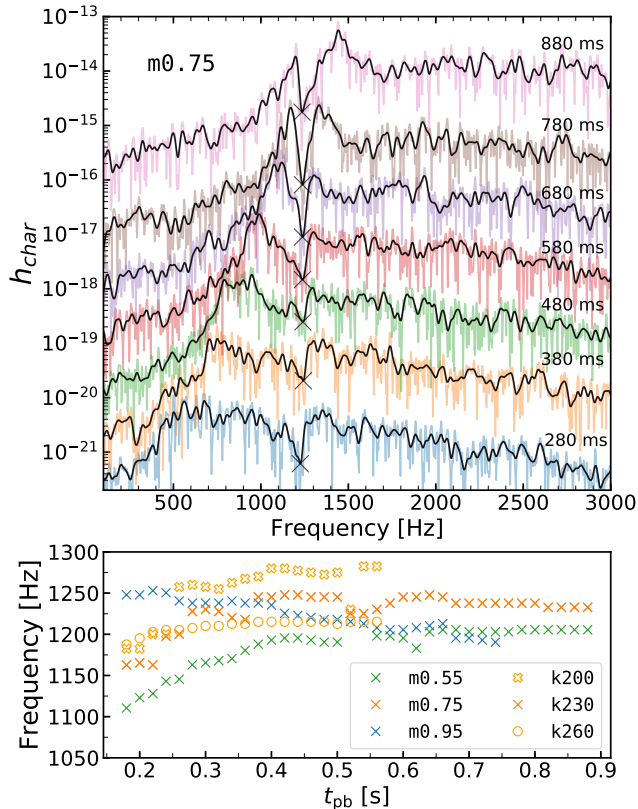


Figure 12. *Top panel:* Characteristic strain (at a 10 kpc distance) calculated for seven times between 280–880 ms post-bounce for the $m0.75$ run (colored lines), with corresponding smoothed versions (black lines). We use a Hann function of 200 ms centered at each time specified, windowing only that section of the GW signal (Figure 2). Each but the first plot is shifted vertically using logarithmically even multiplication factors. This figure provides yet another perspective of the drift of the peak frequency corresponding to the dominant mode frequency. We remark the large dip at ~ 1.2 Hz and mark the local minimum of the smoothed functions which corresponds to the power gap. *Bottom panel:* Applying the same technique to all non-rotating models, we track the frequency of the power gap over many time steps spaced 20 ms apart. In the text we discuss the systematic ordering of the gap with the two EOS parameters and, in general, the central density.

Related to the gap origin suggested by Morozova et al. (2018), other asteroseismology studies see examples of avoided crossings between modes (Torres-Forné et al. 2019b; Sotani & Takiwaki 2020). Torres-Forné et al.

(2019b) introduce mode grouping/classification via the shape of the mode functions, rather than by the number of nodes. With this method, some of their earlier-predicted avoided crossings (when counting nodes) are replaced by plain crossings, shedding light on the exchange of properties when modes cross. If what we see in our simulations is an avoided crossing, perhaps alike the analytical eigenmode solutions in Sotani & Takiwaki (2020), the location of the avoided crossing coincides with the gap (Figure 3). While this is likely no coincidence, and would naturally explain the absence of emission in a small region in the spectrogram (where the modes interact), we have not untangled the process responsible for the power gap which persists during the entire simulation and postpone further investigation to future work. However, our preliminary perturbation analysis yields eigenmodes predicting the two main modes seen in the spectrograms, and further reveals that the $m0.95$ model differs from the others by predicting another avoided crossing at an earlier epoch between less excited modes, a possible explanation for its unique gap morphology. From this preliminary analysis, we also see an eigenmode close to the gap whose energy is mostly confined in the inner core.

For completeness, we remark that the power gap is also evident (and marked with a black dashed line in the projected power spectral density) in the spatially decomposed spectrograms, Figures 10, 13. Other regions lack emission too, which very roughly correspond to nodes from p-modes above the gap and g-modes below (although these are not necessarily eigenmodes but perhaps sporadic wave-like transient perturbations). These “g-mode” nodes appear to converge at the gap, which in principle could produce it.

To finalize our discussion of the power gap we speculate on the reason why some investigations in the literature do not seem to show evidence for this gap (e.g. Mezzacappa et al. 2020; Torres-Forné et al. 2019b; Jardine et al. 2021). Our results, and those of Morozova et al. (2018), show clear evidence that the gap is tied to the physics at the highest densities in the inner ($\lesssim 10$ km) core of the PNS. One potential cause for this disparity is the use of a spherical, 1D, inner core, which prevents aspherical motions, or in this case, potential mode interactions. Morozova et al. (2018); O’Connor & Couch (2018b); Radice et al. (2019) and this work, all see the power gap (or the power gap can be seen in the publicly available data) and do not have such an inner core. The one exception we can find is the work of Pan et al. (2018), who use a very similar setup to our FLASH simulations, but whose published GW spectrograms show no sign of a power gap. On the other hand, several

studies see a much more rich set of isolated excited modes (Torres-Forné et al. 2019b) compared to what is seen in our study. It very well could be that aspects of our numerical setup are enhancing interactions between modes (including the interaction responsible for the power gap), further work still is needed to assess the power gap.

4. CONCLUSIONS

We have presented 9 axisymmetric simulations of CC-SNe where we methodically vary experimentally accessible parameters in the EOS of dense nuclear matter. Our investigation focuses on the effective mass parameter m^* and the incompressibility parameter K_{sat} , allowing values of $m^* \in \{0.55, 0.75, 0.95\}$ and $K_{\text{sat}} \in \{200, 230, 260\}$ MeV baryon $^{-1}$ which represent their estimated mean and 2σ interval. For the values of m^* above and below baseline, the effect of a rotating progenitor is demonstrated using central angular speeds, Ω_0 , of both 1 and 2 rad s $^{-1}$.

In order to investigate the source of GWs and the mechanism which excites the oscillatory perturbations, we have spatially decomposed the GW emission, used linear perturbation analysis, extracted convection zone properties, and provided a thorough discussion of our results in the context of existing literature. First addressed by Morozova et al. (2018), we also report on the power gap and its EOS dependence.

We show that the dominant PNS oscillation mode is heavily dependent on the effective mass and attains a higher frequency when the effective mass parameter is increased. This is due to the more compact PNSs formed for EOSs with higher effective mass, as it affects the thermal pressure during PNS formation (Schneider et al. 2019). As such, the neutrinosphere temperature increases with the effective mass, resulting in higher neutrino/anti-neutrino luminosities and mean energies, and thus, more neutrino heating. Aided by hydrodynamic instabilities like the SASI and convection, this increases the violent neutrino-driven instabilities in the gain region that drive convective overshoot via accretion-plumes striking the PNS. Hence, increasing the effective mass also increases the gravitational wave amplitude and the energy emitted in gravitational waves.

When including rotation, neutrino emission decreases and the gain region is less prone to instabilities. With central angular speeds of $\Omega_0 = 1$ rad s $^{-1}$, the effective mass dependence of the dominant mode frequency is still clearly present, but the GW amplitudes are muted to similar heights. For $\Omega_0 = 2$ rad s $^{-1}$, although differ-

ent effective mass values yield different PNS radii, any clear differences in GWs are washed out by the centrifugally stabilized gain region. These simulations illustrate how rotation affects neutrino quantities and the PNS radii non-linearly. Further studies that allow central angular speeds to vary in value within 1 – 2 rad s $^{-1}$ are encouraged to find a critical value, above which the details of the dominant frequency mode becomes non-distinguishable to observations.

The simulations where K_{sat} varies show no significant differences in neither PNS compactness, PNS convection zone properties, neutrino emission, nor GW signatures. However, as changes in incompressibility can lead to very different *cold*-NS mass-radius relationships, it may be that after a few seconds, once the star has radiated most of its binding energy away in neutrinos, some features in the GW spectra may depend on the isoscalar incompressibility K_{sat} or on the less-constrained isovector incompressibility K_{sym} .

For a distance of 10 kpc, which is a relevant Galactic scale, these 2D CCSNe are detectable with the current generation of laser interferometers. However, recent CCSN studies in 3D highlight that such detections may be marginal for more realistic CCSNe (O’Connor & Couch 2018b; Mezzacappa et al. 2020; Szczepanczyk et al. 2021).

A spatial distribution of the GW emission shows that the dominant emission in our simulations stems from the convectively stable surface layer between densities of $\rho = 10^{11}$ and $\rho = 10^{13}$ g cm $^{-3}$, with a tendency towards the convective overshoot region bordering the convection zone. The emission, which also extends into the convection zone, is in close agreement with a perturbation analysis (Appendix B) suggesting that the GW emission results from coherent quadrupolar oscillatory perturbations of the PNS.

We relay two viable excitation mechanisms of the perturbations (1) accretion plumes onto the PNS surface layer from the post-shock region with which we find a correlation in the GW amplitude via the neutrino heating that, together with the SASI, drives the turbulent convection. This mechanism is established in the literature (e.g. Murphy et al. 2009). And (2) overshoot into the surface layer from the convection zone below. The volume, mass, and kinetic energy inside the convection zone is effective mass dependent, but we find no apparent correlation between these properties and the GW amplitude. Since we see the signatures of overshoot via the turbulent energy flux, we can not rule out this mechanism as a viable forcing of the perturbations, especially in the light of the results of Andresen et al. (2017) and in part Mezzacappa et al. (2020). 3D studies are re-

quired to establish the potency of this mechanism, as it may be washed out by artificially strong excitation from accretion plumes in 2D.

We highlight two analytical procedures that could provide value to future studies in unveiling the mechanism and source of GWs: In Appendix A we remark that caution needs to be taken when calculating the spatial distribution of GWs utilizing the analytic expression for the first time derivative of the quadrupole moment (Eq. 4 in Cartesian and Eq. A5 in spherical coordinates). In Appendix B we highlight that the location where the energy density associated with a particular mode (Torres-Forné et al. 2018; Morozova et al. 2018; Torres-Forné et al. 2019b; Sotani & Takiwaki 2020) is most concentrated, does not necessarily overlap with the region emitting the largest contribution of GWs due to the excitation of that mode.

Related to the origin of GWs is the presence of a narrow ($\Delta f \sim 50$ Hz), high frequency (~ 1.2 kHz), and long lasting region in the spectrograms that lack emission, the “power gap”. We find that the frequency of the power gap changes when varying both the effective mass and the incompressibility modulus, and is generally or-

dered by the value of the central density. This, combined with more detailed arguments (§3.5) and previous analysis of Morozova et al. (2018), strongly hints towards an involvement of the inner core in producing the gap. The modes in the spectrogram appear to undergo an avoided crossing at a frequency coinciding with that of the gap. This is supported by our preliminary perturbation analysis which further indicates that the mode closest to the gap has its energy mostly confined to the inner core.

- 1 We thank Viktoriya Morozova and Michael Pajkos for
- 2 in-depth discussions during the development of this
- 3 work. This work is supported by the Swedish Research
- 4 Council (Project No. 2020-00452). The simulations
- 5 were enabled by resources provided by the Swedish Na-
- 6 tional Infrastructure for Computing (SNIC) at PDC and
- 7 NSC partially funded by the Swedish Research Council
- 8 through grant agreement No. 2016-07213.

Software: FLASH (Fryxell et al. 2000), NuLib (O’Connor 2015), Matplotlib (Hunter 2007), NumPy (Harris et al. 2020), SciPy (Virtanen et al. 2020), yt (Turk et al. 2011)

APPENDIX

A. SPATIAL DISTRIBUTION OF GRAVITATIONAL-WAVE EMISSION

In this Appendix, we give the formulae to acquire the spatial distribution of gravitational-wave (GW) emission. Below we use the spherical coordinate system (r, θ, ϕ) . In axisymmetry, the mass quadrupole moment of a shell centering at r with a thickness of Δr is

$$I_{zz} = \frac{2}{3} \int_{r-\Delta r/2}^{r+\Delta r/2} \rho r'^2 P_2(\cos \theta) dV, \quad (\text{A1})$$

where P_2 is the Legendre polynomial of degree 2, and $dV = r'^2 \sin \theta dr' d\theta d\phi$. According to Eq. 5, the GW strain contributed by this shell is

$$h_+(r, t) = \frac{2}{D} \frac{G}{c^4} \frac{d^2}{dt^2} I_{zz}. \quad (\text{A2})$$

In the main text, we perform numerical differentiation of I_{zz} with respect to t twice to calculate shell contribution $h_+(r, t)$ with $\Delta r = 1$ km. The Fourier transform of $h_+(r, t)$ within a temporal window of 40 ms gives $\tilde{h}_+(r, f)$. In Figure 10 we plot the normalized power $|\tilde{h}_+(r, f)|^2$ as radial profiles of the GW spectrogram.

Generally, one wants to avoid numerical differentiation to minimize numerical noise (Finn & Evans 1990). With the mass conservation equation $\frac{\partial \rho}{\partial t} + \nabla \cdot (\rho \vec{v}) = 0$, one can avoid the first numerical differentiation of I_{zz} as

$$\frac{dI_{zz}}{dt} = \frac{2}{3} \int_{r-\Delta r/2}^{r+\Delta r/2} \frac{\partial \rho}{\partial t} r'^2 P_2(\cos \theta) dV = -\frac{2}{3} \int_{r-\Delta r/2}^{r+\Delta r/2} \nabla \cdot (\rho \vec{v}) r'^2 P_2(\cos \theta) dV. \quad (\text{A3})$$

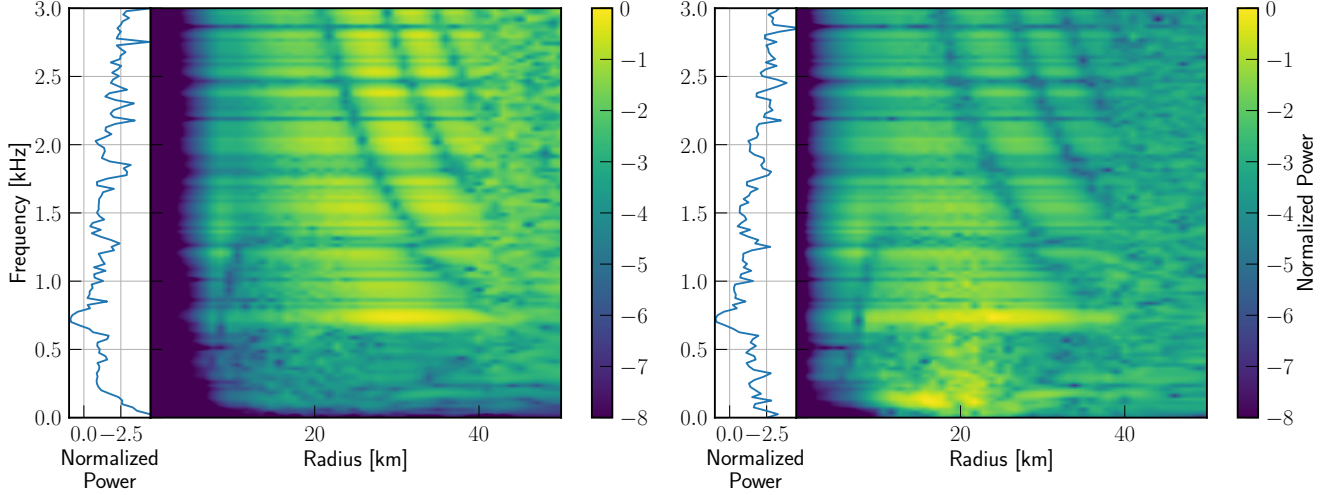


Figure 13. Radial profiles of GW spectrograms at $t = 0.4$ s after bounce calculated by numerical differentiation of I_{zz} (left panel) and dI_{zz}/dt without the surface term (right panel).

Partial integration is used to further avoid the spatial differentiation. For example, the radial derivative can be avoided by

$$\left(\frac{dI_{zz}}{dt}\right)_r = -\frac{2}{3} \int_0^{2\pi} d\phi \int_0^\pi P_2(\cos\theta) \sin\theta d\theta \int_{r-\Delta r/2}^{r+\Delta r/2} \frac{\partial}{\partial r'} (r'^2 \rho v_r) r'^2 dr' \quad (\text{A4})$$

$$= -\frac{2}{3} \int_0^{2\pi} d\phi \int_0^\pi P_2(\cos\theta) \sin\theta d\theta \left(r'^4 \rho v_r \Big|_{r-\Delta r/2}^{r+\Delta r/2} - 2 \int_{r-\Delta r/2}^{r+\Delta r/2} r'^3 \rho v_r dr' \right). \quad (\text{A5})$$

Note that there is a surface term $r'^4 \rho v_r \Big|_{r-\Delta r/2}^{r+\Delta r/2}$ from the partial integration. This term can be ignored when calculating dI_{zz}/dt of the whole star, because it vanishes at $r = 0$ and at the stellar surface where $\rho = 0$. However, the surface term cannot be dropped for an arbitrary mass shell. In Figure 13 we compare the spatial GW spectrogram evaluated by numerical differentiation of I_{zz} (left panel) and dI_{zz}/dt (right panel) calculated as

$$\frac{dI_{zz}}{dt} = \frac{2}{3} \int_{r-\Delta r/2}^{r+\Delta r/2} \rho r' \left(2v_r P_2(\cos\theta) + v_\theta \frac{\partial P_2(\cos\theta)}{\partial\theta} \right) dV, \quad (\text{A6})$$

where the surface terms are ignored. Though the total GW emission is not affected due to canceling of the surface terms (except for the noise due to numerical differentiation), the detailed spatial distribution is clearly different. This comparison shows that using Eq. A6 can lead to a problematic results in the spatial contribution to GW emission, especially if Δr is small.

B. COMPARISON BETWEEN SIMULATION AND PERTURBATION ANALYSIS

We follow [Westernacher-Schneider \(2020\)](#) to perform a perturbation analysis which is consistent with our pseudo-Newtonian hydrodynamic simulations. Eqs. 3.12-3.15 in [Westernacher-Schneider \(2020\)](#) are solved with a 4-stage Runge-Kutta method to get the quadrupolar ($l = 2$) perturbative mode functions, namely, the radial displacement η_r , tangential displacement η_\perp , and density $\delta\hat{\rho}$ as a function of radii. Here, we do not fix the outer boundary condition to get the eigenmodes, but set the mode frequency in the perturbative equations to be the peak GW frequency and acquire the corresponding mode functions for the background fluid at a specific time. The perturbative quadrupole moment responsible for GW emission is

$$\delta Q = \int r^4 \delta\hat{\rho} dr. \quad (\text{B7})$$

In the top panel of Figure 14 we compare the radial profiles of GW emission ($\tilde{h}_+(r, f)$ in Appendix A) in the simulations with $Cr^4\delta\hat{\rho}$ from the perturbation analysis, where a multiplication constant C is used to match the maximums between

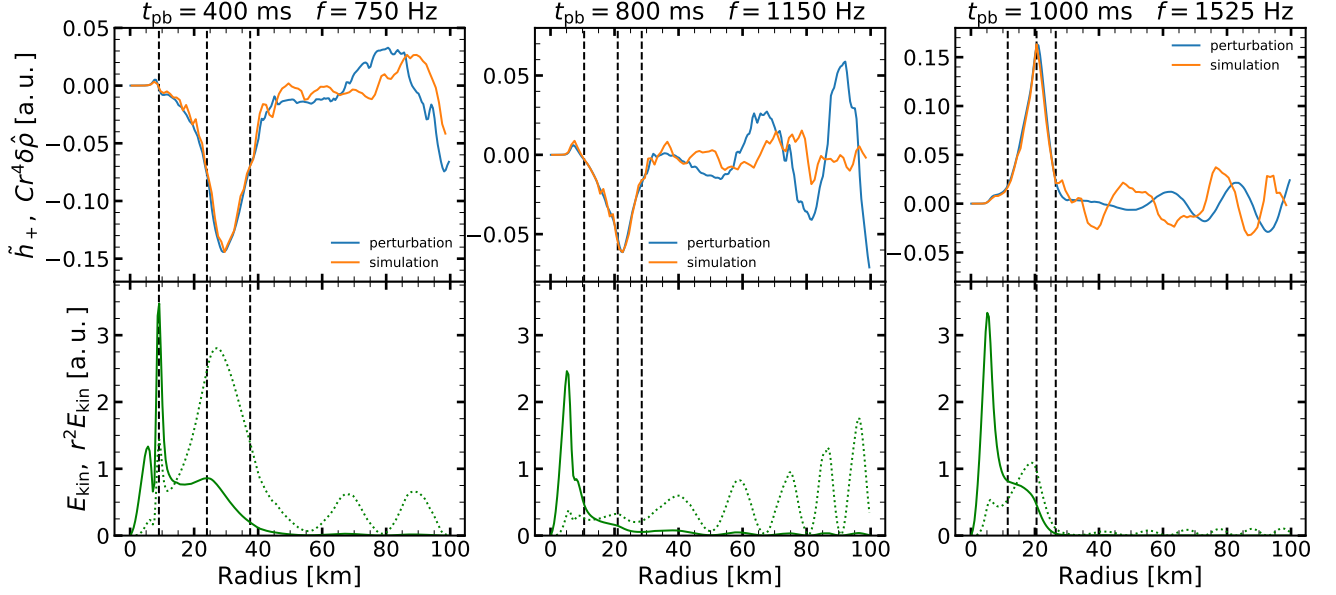


Figure 14. Comparison between perturbation analysis and simulations with $m^* = 0.75$, for GW peak frequencies at $t = 400, 800, 1000$ ms after bounce, from left to right. *Top panel:* simulation is $\tilde{h}_+(r, f)$ described in Appendix A and perturbation is $Cr^4\delta\hat{\rho}$ in Eq. B7. *Bottom panel:* solid line is E_{kin} in Eq. B8 and dashed line is scaled r^2E_{kin} . Vertical black dashed lines in each panel are locations of $\rho = 2 \times 10^{14}, 10^{13}, 10^{11}$ g cm $^{-3}$, from left to right.

them. Agreement is found inside the PNS ($\rho \geq 10^{11}$ g cm $^{-3}$), suggesting that GW emission results from the coherent quadrupolar oscillations of the entire PNS. In the bottom panel of Figure 14 we plot the radial profiles of the kinetic energy density of the perturbative mode as (Eq. 59 in Torres-Forné et al. 2019b)

$$E_{\text{kin}} = \rho \left[\eta_r^2 + l(l+1) \left(\frac{\eta_\perp}{r} \right)^2 \right], \quad (\text{B8})$$

where $l = 2$. Similar to Torres-Forné et al. (2019b); Morozova et al. (2018), the kinetic energy density has its maximum inside the inner core (~ 10 km). However, the kinetic energy which has a r^2 from the volume dV resembles the distribution of GW emission (except for the leakage to outside PNS at $t_{\text{pb}} = 800$ ms). We assert from this that using the energy density alone to quantify the location of GW emission is inappropriate. Details on the perturbation analysis such as eigenmodes analysis is still under investigation and will be described elsewhere.

REFERENCES

- Abbott, B. P., Abbott, R., Abbott, T. D., et al. 2016, *ApJL*, 818, L22, doi: [10.3847/2041-8205/818/2/L22](https://doi.org/10.3847/2041-8205/818/2/L22)
- . 2017, *PhRvL*, 119, 161101, doi: [10.1103/PhysRevLett.119.161101](https://doi.org/10.1103/PhysRevLett.119.161101)
- Adams, S. M., Kochanek, C. S., Beacom, J. F., Vagins, M. R., & Stanek, K. Z. 2013, *ApJ*, 778, 164, doi: [10.1088/0004-637X/778/2/164](https://doi.org/10.1088/0004-637X/778/2/164)
- Andresen, H., Müller, B., Müller, E., & Janka, H. T. 2017, *MNRAS*, 468, 2032, doi: [10.1093/mnras/stx618](https://doi.org/10.1093/mnras/stx618)
- Andresen, H., Müller, E., Janka, H. T., et al. 2019, *MNRAS*, 486, 2238, doi: [10.1093/mnras/stz990](https://doi.org/10.1093/mnras/stz990)
- Barsotti, L., Gras, S., Evans, M., & Fritschel, P. 2018, Tech. Rep. LIGO-T1800042-v5
- Betranhandy, A., & O’Connor, E. 2020, *PhRvD*, 102, 123015, doi: [10.1103/PhysRevD.102.123015](https://doi.org/10.1103/PhysRevD.102.123015)
- Blanchet, L., Damour, T., & Schaefer, G. 1990, *MNRAS*, 242, 289, doi: [10.1093/mnras/242.3.289](https://doi.org/10.1093/mnras/242.3.289)
- Bruenn, S. W. 1985, *ApJS*, 58, 771, doi: [10.1086/191056](https://doi.org/10.1086/191056)
- Burrows, A., Reddy, S., & Thompson, T. A. 2006, *NuPhA*, 777, 356. <https://arxiv.org/abs/astro-ph/0404432>
- Cerdá-Durán, P., DeBrye, N., Aloy, M. A., Font, J. A., & Obergaulinger, M. 2013, *ApJL*, 779, L18, doi: [10.1088/2041-8205/779/2/L18](https://doi.org/10.1088/2041-8205/779/2/L18)
- Constantinou, C., Muccioli, B., Prakash, M., & Lattimer, J. M. 2014, *PhRvC*, 89, 065802, doi: [10.1103/PhysRevC.89.065802](https://doi.org/10.1103/PhysRevC.89.065802)

- Couch, S. M. 2013, *ApJ*, 765, 29,
doi: [10.1088/0004-637X/765/1/29](https://doi.org/10.1088/0004-637X/765/1/29)
- Couch, S. M., & O'Connor, E. P. 2014, *ApJ*, 785, 123,
doi: [10.1088/0004-637X/785/2/123](https://doi.org/10.1088/0004-637X/785/2/123)
- Couch, S. M., & Ott, C. D. 2015, *ApJ*, 799, 5,
doi: [10.1088/0004-637X/799/1/5](https://doi.org/10.1088/0004-637X/799/1/5)
- Danielewicz, P., Lacey, R., & Lynch, W. G. 2002, *Science*, 298, 1592, doi: [10.1126/science.1078070](https://doi.org/10.1126/science.1078070)
- Finn, L. S., & Evans, C. R. 1990, *ApJ*, 351, 588,
doi: [10.1086/168497](https://doi.org/10.1086/168497)
- Fryxell, B., Olson, K., Ricker, P., et al. 2000, *ApJS*, 131, 273, doi: [10.1086/317361](https://doi.org/10.1086/317361)
- Gossan, S. E., Fuller, J., & Roberts, L. F. 2020, *MNRAS*, 491, 5376, doi: [10.1093/mnras/stz3243](https://doi.org/10.1093/mnras/stz3243)
- Handler, G. 2013, *Asteroseismology*, ed. T. D. Oswalt & M. A. Barstow, Vol. 4, 207,
doi: [10.1007/978-94-007-5615-1_4](https://doi.org/10.1007/978-94-007-5615-1_4)
- Hannestad, S., & Raffelt, G. 1998, *ApJ*, 507, 339,
doi: [10.1086/306303](https://doi.org/10.1086/306303)
- Harris, C. R., Millman, K. J., van der Walt, S. J., et al. 2020, *Nature*, 585, 357, doi: [10.1038/s41586-020-2649-2](https://doi.org/10.1038/s41586-020-2649-2)
- Hempel, M., Oertel, M., Typel, S., & Klähn, T. 2017, in 14th International Symposium on Nuclei in the Cosmos (NIC2016), ed. S. Kubono, T. Kajino, S. Nishimura, T. Isobe, S. Nagataki, T. Shima, & Y. Takeda, 010802, doi: [10.7566/JPSCP.14.010802](https://doi.org/10.7566/JPSCP.14.010802)
- Horowitz, C. J. 2002, *PhRvD*, 65, 043001,
doi: [10.1103/PhysRevD.65.043001](https://doi.org/10.1103/PhysRevD.65.043001)
- Hunter, J. D. 2007, *Computing In Science & Engineering*, 9, 90
- Janka, H.-T. 2017, *Neutrino-Driven Explosions*, ed. A. W. Alsabti & P. Murdin, 1095,
doi: [10.1007/978-3-319-21846-5_109](https://doi.org/10.1007/978-3-319-21846-5_109)
- Jardine, R., Powell, J., & Müller, B. 2021, arXiv e-prints, arXiv:2105.01315. <https://arxiv.org/abs/2105.01315>
- Kaplan, J. D., Ott, C. D., O'Connor, E. P., et al. 2014, *ApJ*, 790, 19, doi: [10.1088/0004-637X/790/1/19](https://doi.org/10.1088/0004-637X/790/1/19)
- Kuroda, T., Kotake, K., Hayama, K., & Takiwaki, T. 2017, *ApJ*, 851, 62, doi: [10.3847/1538-4357/aa988d](https://doi.org/10.3847/1538-4357/aa988d)
- Lattimer, J. M., Pethick, C. J., Ravenhall, D. G., & Lamb, D. Q. 1985, *Nucl. Phys. A*, 432, 646 ,
doi: [http://dx.doi.org/10.1016/0375-9474\(85\)90006-5](http://dx.doi.org/10.1016/0375-9474(85)90006-5)
- Lattimer, J. M., & Swesty, D. F. 1991, *NuPhA*, 535, 331,
doi: [10.1016/0375-9474\(91\)90452-C](https://doi.org/10.1016/0375-9474(91)90452-C)
- Li, W., Chornock, R., Leaman, J., et al. 2011, *MNRAS*, 412, 1473, doi: [10.1111/j.1365-2966.2011.18162.x](https://doi.org/10.1111/j.1365-2966.2011.18162.x)
- Marek, A., Dimmelmeier, H., Janka, H. T., Müller, E., & Buras, R. 2006, *A&A*, 445, 273,
doi: [10.1051/0004-6361:20052840](https://doi.org/10.1051/0004-6361:20052840)
- Marek, A., Janka, H. T., & Müller, E. 2009, *A&A*, 496, 475, doi: [10.1051/0004-6361/200810883](https://doi.org/10.1051/0004-6361/200810883)
- Margueron, J., Hoffmann Casali, R., & Gulminelli, F. 2018, *PhRvC*, 97, 025805, doi: [10.1103/PhysRevC.97.025805](https://doi.org/10.1103/PhysRevC.97.025805)
- Mezzacappa, A., Marronetti, P., Landfield, R. E., et al. 2020, *PhRvD*, 102, 023027,
doi: [10.1103/PhysRevD.102.023027](https://doi.org/10.1103/PhysRevD.102.023027)
- Morozova, V., Radice, D., Burrows, A., & Vartanyan, D. 2018, *ApJ*, 861, 10, doi: [10.3847/1538-4357/aac5f1](https://doi.org/10.3847/1538-4357/aac5f1)
- Müller, B. 2015, *MNRAS*, 453, 287,
doi: [10.1093/mnras/stv1611](https://doi.org/10.1093/mnras/stv1611)
- Müller, B., Janka, H.-T., & Marek, A. 2013, *ApJ*, 766, 43,
doi: [10.1088/0004-637X/766/1/43](https://doi.org/10.1088/0004-637X/766/1/43)
- Müller, E., Janka, H. T., & Wongwathanarat, A. 2012, *A&A*, 537, A63, doi: [10.1051/0004-6361/201117611](https://doi.org/10.1051/0004-6361/201117611)
- Murphy, J. W., Dolence, J. C., & Burrows, A. 2013, *ApJ*, 771, 52, doi: [10.1088/0004-637X/771/1/52](https://doi.org/10.1088/0004-637X/771/1/52)
- Murphy, J. W., Ott, C. D., & Burrows, A. 2009, *ApJ*, 707, 1173, doi: [10.1088/0004-637X/707/2/1173](https://doi.org/10.1088/0004-637X/707/2/1173)
- O'Connor, E. 2015, *ApJS*, 219, 24,
doi: [10.1088/0067-0049/219/2/24](https://doi.org/10.1088/0067-0049/219/2/24)
- O'Connor, E., & Ott, C. D. 2011, *ApJ*, 730, 70,
doi: [10.1088/0004-637X/730/2/70](https://doi.org/10.1088/0004-637X/730/2/70)
- O'Connor, E. P., & Couch, S. M. 2018a, *ApJ*, 865, 81,
doi: [10.3847/1538-4357/aadcf7](https://doi.org/10.3847/1538-4357/aadcf7)
- . 2018b, *ApJ*, 854, 63, doi: [10.3847/1538-4357/aaa893](https://doi.org/10.3847/1538-4357/aaa893)
- Oertel, M., Hempel, M., Klähn, T., & Typel, S. 2017, *Reviews of Modern Physics*, 89, 015007,
doi: [10.1103/RevModPhys.89.015007](https://doi.org/10.1103/RevModPhys.89.015007)
- Pajkos, M. A., Couch, S. M., Pan, K.-C., & O'Connor, E. P. 2019, *ApJ*, 878, 13, doi: [10.3847/1538-4357/ab1de2](https://doi.org/10.3847/1538-4357/ab1de2)
- Pan, K.-C., Liebendörfer, M., Couch, S. M., & Thielemann, F.-K. 2018, *ApJ*, 857, 13, doi: [10.3847/1538-4357/aab71d](https://doi.org/10.3847/1538-4357/aab71d)
- Powell, J., & Müller, B. 2019, *MNRAS*, 487, 1178,
doi: [10.1093/mnras/stz1304](https://doi.org/10.1093/mnras/stz1304)
- Prakash, M., Bombaci, I., Prakash, M., et al. 1997, *PhR*, 280, 1, doi: [10.1016/S0370-1573\(96\)00023-3](https://doi.org/10.1016/S0370-1573(96)00023-3)
- Radice, D., Morozova, V., Burrows, A., Vartanyan, D., & Nagakura, H. 2019, *ApJL*, 876, L9,
doi: [10.3847/2041-8213/ab191a](https://doi.org/10.3847/2041-8213/ab191a)
- Reisswig, C., Ott, C. D., Sperhake, U., & Schnetter, E. 2011, *PhRvD*, 83, 064008,
doi: [10.1103/PhysRevD.83.064008](https://doi.org/10.1103/PhysRevD.83.064008)
- Scheidegger, S., Käppeli, R., Whitehouse, S. C., Fischer, T., & Liebendörfer, M. 2010, *A&A*, 514, A51,
doi: [10.1051/0004-6361/200913220](https://doi.org/10.1051/0004-6361/200913220)
- Schneider, A., O'Connor, E., Granqvist, E., Betranhandy, A., & Couch, S. M. 2020, *ApJ*, 894, 4,
doi: [10.3847/1538-4357/ab8308](https://doi.org/10.3847/1538-4357/ab8308)

- Schneider, A. S., Roberts, L. F., & Ott, C. D. 2017, *PhRvC*, 96, 065802, doi: [10.1103/PhysRevC.96.065802](https://doi.org/10.1103/PhysRevC.96.065802)
- Schneider, A. S., Roberts, L. F., Ott, C. D., & O'Connor, E. 2019, *PhRvC*, 100, 055802, doi: [10.1103/PhysRevC.100.055802](https://doi.org/10.1103/PhysRevC.100.055802)
- Sotani, H., & Takiwaki, T. 2020, *MNRAS*, 498, 3503, doi: [10.1093/mnras/staa2597](https://doi.org/10.1093/mnras/staa2597)
- Summa, A., Janka, H.-T., Melson, T., & Marek, A. 2018, *ApJ*, 852, 28, doi: [10.3847/1538-4357/aa9ce8](https://doi.org/10.3847/1538-4357/aa9ce8)
- Szczepanczyk, M., Antelis, J., Benjamin, M., et al. 2021, arXiv e-prints, arXiv:2104.06462. <https://arxiv.org/abs/2104.06462>
- Takiwaki, T., & Kotake, K. 2018, *MNRAS*, 475, L91, doi: [10.1093/mnrasl/sly008](https://doi.org/10.1093/mnrasl/sly008)
- Torres-Forné, A., Cerdá-Durán, P., Obergaulinger, M., Müller, B., & Font, J. A. 2019a, *PhRvL*, 123, 051102, doi: [10.1103/PhysRevLett.123.051102](https://doi.org/10.1103/PhysRevLett.123.051102)
- Torres-Forné, A., Cerdá-Durán, P., Passamonti, A., & Font, J. A. 2018, *MNRAS*, 474, 5272, doi: [10.1093/mnras/stx3067](https://doi.org/10.1093/mnras/stx3067)
- Torres-Forné, A., Cerdá-Durán, P., Passamonti, A., Obergaulinger, M., & Font, J. A. 2019b, *MNRAS*, 482, 3967, doi: [10.1093/mnras/sty2854](https://doi.org/10.1093/mnras/sty2854)
- Turk, M. J., Smith, B. D., Oishi, J. S., et al. 2011, *The Astrophysical Journal Supplement Series*, 192, 9, doi: [10.1088/0067-0049/192/1/9](https://doi.org/10.1088/0067-0049/192/1/9)
- Virtanen, P., Gommers, R., Oliphant, T. E., et al. 2020, *Nature Methods*, 17, 261, doi: [10.1038/s41592-019-0686-2](https://doi.org/10.1038/s41592-019-0686-2)
- Westernacher-Schneider, J. R. 2020, *PhRvD*, 101, 083021, doi: [10.1103/PhysRevD.101.083021](https://doi.org/10.1103/PhysRevD.101.083021)
- Westernacher-Schneider, J. R., O'Connor, E., O'Sullivan, E., et al. 2019, *PhRvD*, 100, 123009, doi: [10.1103/PhysRevD.100.123009](https://doi.org/10.1103/PhysRevD.100.123009)
- Woosley, S. E., & Heger, A. 2007, *PhR*, 442, 269, doi: [10.1016/j.physrep.2007.02.009](https://doi.org/10.1016/j.physrep.2007.02.009)
- Xiao, Z., Wan, M., Chen, S., & Eyink, G. L. 2009, *Journal of Fluid Mechanics*, 619, 1–44, doi: [10.1017/S0022112008004266](https://doi.org/10.1017/S0022112008004266)
- Yakunin, K. N., Mezzacappa, A., Marronetti, P., et al. 2015, *PhRvD*, 92, 084040, doi: [10.1103/PhysRevD.92.084040](https://doi.org/10.1103/PhysRevD.92.084040)
- Yasin, H., Schäfer, S., Arcones, A., & Schwenk, A. 2020, *Phys. Rev. Lett.*, 124, 092701, doi: [10.1103/PhysRevLett.124.092701](https://doi.org/10.1103/PhysRevLett.124.092701)
- Zha, S., O'Connor, E. P., Chu, M.-c., Lin, L.-M., & Couch, S. M. 2020, *PhRvL*, 125, 051102, doi: [10.1103/PhysRevLett.125.051102](https://doi.org/10.1103/PhysRevLett.125.051102)